01 Jan 2023

Advances in Fiber-Optic Extrinsic Fabry-Perot Interferometric Physical and Mechanical Sensors: A Review

Chen Zhu

Hongkun Zheng

Lingmei Ma

Zheyi Yao

et. al. For a complete list of authors, see https://scholarsmine.mst.edu/ele_comeng_facwork/4738

Recommended Citation

C. Zhu et al., "Advances in Fiber-Optic Extrinsic Fabry-Perot Interferometric Physical and Mechanical Sensors: A Review," *IEEE Sensors Journal*, Institute of Electrical and Electronics Engineers, Jan 2023. The definitive version is available at https://doi.org/10.1109/JSEN.2023.3244820

Advances in Fiber-Optic Extrinsic Fabry-Perot Interferometric Physical and Mechanical Sensors: A Review

Chen Zhu, *Member, IEEE*, Hongkun Zheng, Lingmei Ma, Zheyi Yao, Bo Liu, Jie Huang, *Senior Member, IEEE*, Yunjiang Rao, *Fellow, IEEE*

***Abstract*—Fabry-Perot interferometers have found a multitude of scientific and industrial applications ranging from gravitational wave detection, high-resolution spectroscopy, and optical filters to quantum optomechanics. Integrated with optical fiber waveguide technology, the fiber-optic Fabry-Perot interferometers have emerged as a unique candidate for high-sensitivity sensing and have undergone tremendous growth and advancement in the past two decades with their successful applications in an expansive range of fields. The extrinsic cavity-based devices, i.e., the fiber-optic extrinsic Fabry-Perot interferometers (EFPIs), enable great flexibility in the design of the sensitive Fabry-Perot cavity combined with state-of-the-art micromachining and conventional mechanical fabrication, leading to the development of a diverse array of EFPI sensors targeting at different physical quantities. Here, we summarize the recent progress of fiber-optic EFPI sensors, providing an overview of different physical and mechanical sensors based on the Fabry-Perot interferometer principle, with a special focus on displacement-related quantities, such as strain, force, tilt, vibration and acceleration, pressure, and acoustic. The working principle and signal demodulation methods are shown in brief. Perspectives on further advancement of EFPI sensing technologies are also discussed.**

***Index Terms*—Fabry-Perot interferometer; extrinsic Fabry-Perot interferometer; fiber-optic sensor; interferometer; physical and mechanical sensor.**

I. Introduction

SINCE its first report in 1897 by the physicists Charles Fabry and Alfred Perot [1], the Fabry-Perot interferometer (FPI) has played a very important role in various optical fields [2], such as lasers [3-5], filters [6-8], and sensors [9-11]. Of particular relevance here, fiber-optic FPI sensors have attracted wide attention and have undergone tremendous growth in the past decades [9, 12, 13]. Fiber-optic sensors in general have some unique advantages over conventional electrical sensors, such as immunity to electromagnetic interference, corrosion resistance, small size, etc. Among a large number of fiber-optic sensors, e.g., fiber Bragg gratings (FBGs), long-period gratings, and various interferometric sensors, the FPI is especially advantageous in terms of fabrication complexity and cost.

The research of Chen Zhu was supported by the Research Initiation Project of Zhejiang Lab (2022ME0PI01). The research was also supported in part by the Key Research Project of Zhejiang Lab (2020MEOAD02).

Chen Zhu, Hongkun Zheng, Lingmei Ma, and Bo Liu are with the Research Center for Optical Fiber Sensing, Zhejiang Laboratory, Hangzhou 311100, China. (Corresponding author: Chen Zhu, chenzhu@zhejianglab.com)

Zheyi Yao is with the School of Electronic Engineering and Optoelectronic Technology, Nanjing University of Science and Technology, Nanjing 210094, China.

Jie Huang is with the Department of Electrical and Computer Engineering, Missouri University of Science and Technology, Rolla, MO 65409, USA.

Yunjiang Rao is with the Research Center for Optical Fiber Sensing, Zhejiang Laboratory, Hangzhou 311100, China, and is also with the Key Laboratory of Optical Fiber Sensing & Communications, University of Electronic Science & Technology of China, Chengdu, Sichuan 611731, China.

The FPI structure is arguably one of the simplest and most widely explored configurations in developing compact fiber-optic sensors [9, 12]. An FPI typically consists of a cavity formed between two optical reflectors, the so-called Fabry-Perot cavity. The FPI sensors reported in the literature can be generally classified into two categories, the intrinsic FPI (IFPI)-based and the extrinsic FPI (EFPI)-based. In the case of the IFPI, the Fabry-Perot cavity is formed between two fiber in-line reflectors with a solid cavity (i.e., the fiber between the two reflectors), as shown in Fig. 1(a). Since fiber in-line reflectors are required, micromachining processes are involved in the construction of an IFPI-based sensor device, such as femtosecond laser micromachining and fusion splicing. A detailed overview of IFPI-based sensors can be found in [14]. For the EFPI, the Fabry-Perot cavity is formed between the fiber tip with a cleaved end facet and an external reflector with the air in-between serving as the cavity medium, where no high-precision micro-fabrication is needed. On one hand, as shown in Fig. 1(b), an optical fiber with its cleaved end facet can serve as the external reflector and a capillary tube can be used as the common fixture of the two fibers. On the other hand, as shown in Fig. 1(c), a separate mirror positioned a certain distance away from the end facet of the lead-in fiber can be used as the external reflector where the fiber and the mirror can be fixed to different structures to form the Fabry-Perot cavity. Alternatively, a thin film of material of interest can be deposited onto the cleaved end facet of an optical fiber to form an EFPI, where the interface between the optical fiber and the material acts as the first reflector, and the interface between the material and ambient environment acts as the second reflector,

as schematically illustrated in Fig. 1(d). Each of the IFPI and EFPI sensor devices has its own merit, and a chronology of the development of FPI sensors can be found in [12].

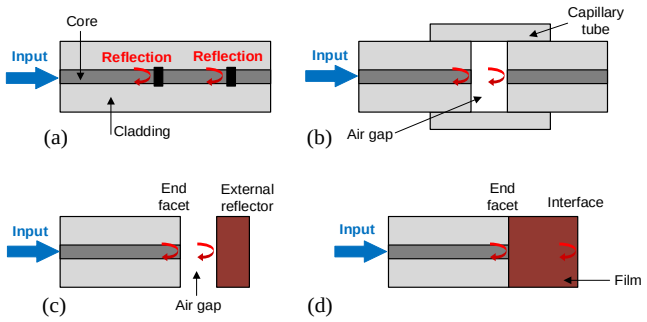

Fig. 1. Schematic of various fiber-optic FPI configurations. (a) IFPI with a solid cavity. (b) EFPI with an air-gap cavity constructed with the assistance of a capillary tube. (c) EFPI with a free-space external reflector and an air-gap cavity. (d) EFPI with a film deposited on the end facet of the optical fiber with a solid cavity.

In this work, we focus on reviewing the recent progress of air-gap EFPI-based sensors, i.e., the configurations shown in Fig. 1(b) and 1(c). In later discussion, EFPI is referred to as the air-gap EFPI. The selection is justified as follows. The EFPI structure is very easy to fabricate, and its long-term stability and reliability are ensured due to the air-gap-based cavity, making it suitable for cyclic loading conditions. Also, since the air gap is introduced as the cavity medium, the EFPI has a small temperature cross-talk effect thanks to the small thermo-optic coefficient of air. Moreover, the extrinsic structure endows it with the capability for responding to a wide variety of measurands and therefore making it an ultra-flexible platform for developing various sensors by combining with both advanced (micromachined) and conventional mechanical transducers. Additionally, with the development of the white light interferometry interrogation technique, the cavity length of an EFPI device can be resolved to a sub-nanometer scale. Therefore, a great number of high-sensitivity EFPI sensors for measuring different physical quantities have been developed in the past decade. Note that a few review articles reporting miniature and fiber in-line FPI sensors can be found in the literature [9, 12, 15]. This paper aims to summarize, for the first time, the recent significant efforts in developing highly sensitive EFPI sensors with the assistance of judicious mechanical transducers. We believe that this study will show the readers that ultra-high-performance sensor devices can be developed by simply employing one of the simplest principles (i.e., the FPI principle) combined with easy and low-cost fabrication processes. We hope that the work present herein will open new avenues and inspire researchers in the field of sensing to develop new generations of sensors with improved performance and yet reduced system cost.

The article is organized as follows. Section II reviews the working principle and simplified model of the EFPI device, where the demodulation algorithms developed for EFPI sensors are also briefly discussed. Section III discusses different EFPI sensors in the literature categorized based on the measurand of interest. Challenges and future perspectives in further research on the advancement of FPI sensing technologies are given in Section IV. Section V concludes this paper.

II. EFPI Device

Since the air-gap EFPI device consists of a cavity formed between two optical reflectors, the light field circulates back and forth in the Fabry-Perot cavity with round trip time determined by the cavity length and the refractive index of the cavity medium (i.e., the air in this case). Thus, multiple reflections have to be taken into consideration for deriving the mathematical model of an EFPI device. However, since the first reflector of an EPFI sensor is typically the interface between the optical fiber end facet and air, which is smaller than 4%, multiple trips of the light can be simplified as a single round trip in the cavity. As a result, a two-beam interference model can be used to describe a low-finesse EFPI device. The total reflection will be the superposition of the two reflected signals from the first reflector (i.e., the fiber-air interface) and the second reflector (i.e., the external reflector), as illustrated in Fig. 2(a). The total reflection can be expressed as

$$I = I_1 + I_2 + 2\sqrt{I_1 I_2}\cos(\varphi + \varphi_0) \tag{1}$$

where I_1 and I_2 are the reflected light intensities at the fiber-air interface and the external reflector, respectively; φ_0 is the additional phase introduced by the second reflector; and, φ denotes the round-trip phase delay introduced by the Fabry-Perot cavity and is given by

$$\varphi = \frac{4\pi nL}{\lambda} \tag{2}$$

where n represents the refractive index of the cavity medium and can be considered constant for air, i.e., n = 1; L is the physical length of the Fabry-Perot cavity, i.e., the distance between the two reflectors; and, λ is the wavelength of the probing light.

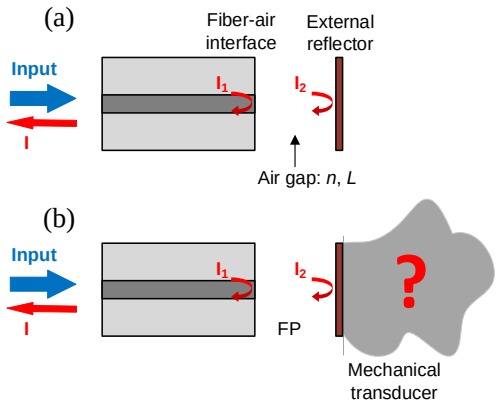

Fig. 2. Illustration of an EFPI device. (a) Simplified two-beam interference model for an EFPI device. (b) Illustration of an EFPI as a universal platform in combination with a mechanical transducer for developing ultra-sensitive sensors.

Combining Eqs. (1) and (2), one can conclude that changes in the cavity length of the Fabry-Perot cavity results in changes in the total reflected power of the EFPI. By tracking the variation of the reflection of an EFPI sensor, the subtle change in the cavity length caused by external perturbation can be quantified. Thus, the intensity-based scheme was developed for the demodulation of EFPI sensors, where a single-wavelength

laser working at the quasi-linear point in the sinusoidal spectrum (i.e., the quadrature point) was employed [16-18]. The intensity-based interrogation system has a fast update rate, a simple system structure, and is low in cost. However, due to the intrinsic periodic interference pattern, the dynamic range of intensity-based EFPI sensors is strictly limited ($< \lambda/4$). Also, additional hardware is required to eliminate the intensity fluctuation of the probing light and the drift of the quadrature point. With the development of white light interferometry, direct calculation of the cavity length from the reflected interferogram has become one of the most widely used demodulation approaches for EFPI sensors [19-22]. A variety of algorithms have been explored for the accurate determination of the absolute cavity length of EFPI sensors, and can be generally divided into three types: Fourier transform-based, multiple peak tracking, and cross-correlation-based methods. Other methods include single-peak tracking and quadrature-phase demodulation methods. A detailed review of these algorithms can be found in recent review articles [13, 23]. The absolute cavity length demodulation method provides much richer information among different approaches and is robust against the system and environmental noise.

Based on the advanced algorithms, the change in the cavity length of an EFPI device can be resolved to the sub-nanometer scale. The integration of an EFPI device with a judicious mechanical design offers a universal strategy to develop a new generation of ultra-sensitive fiber-optic sensors, as conceptually illustrated in Fig. 2(b). Any physical parameter that can be correlated to the movement (displacement and deflection) of the external reflector (via the mechanical transducer) can be measured using an EFPI sensor. The next section discusses the recently developed high-sensitivity EFPI sensors. Note that in addition to physical and mechanical sensing, another important application field of fiber-optic sensors is chemical and biological sensing [24-41]. The FPI configuration can also be employed for chemical and biological sensing by encoding the measurand of interest to variations of the refractive index of its cavity medium [42-44]. This aspect is beyond the scope of this paper.

III. EFPI Sensors

1. Displacement Sensors

Displacement is one of the basic physical parameters in various fields and applications [45]. The successful development of displacement sensors gives us the opportunity to design sensor devices for measuring a diverse array of quantities that can be easily correlated to displacement, e.g., pressure, acoustic wave, acceleration, vibration, etc. Moreover, the EFPI device is a promising candidate for displacement sensing because of its external and free-space cavity and its capability to resolve changes in the cavity length to a sub-nanometer scale.

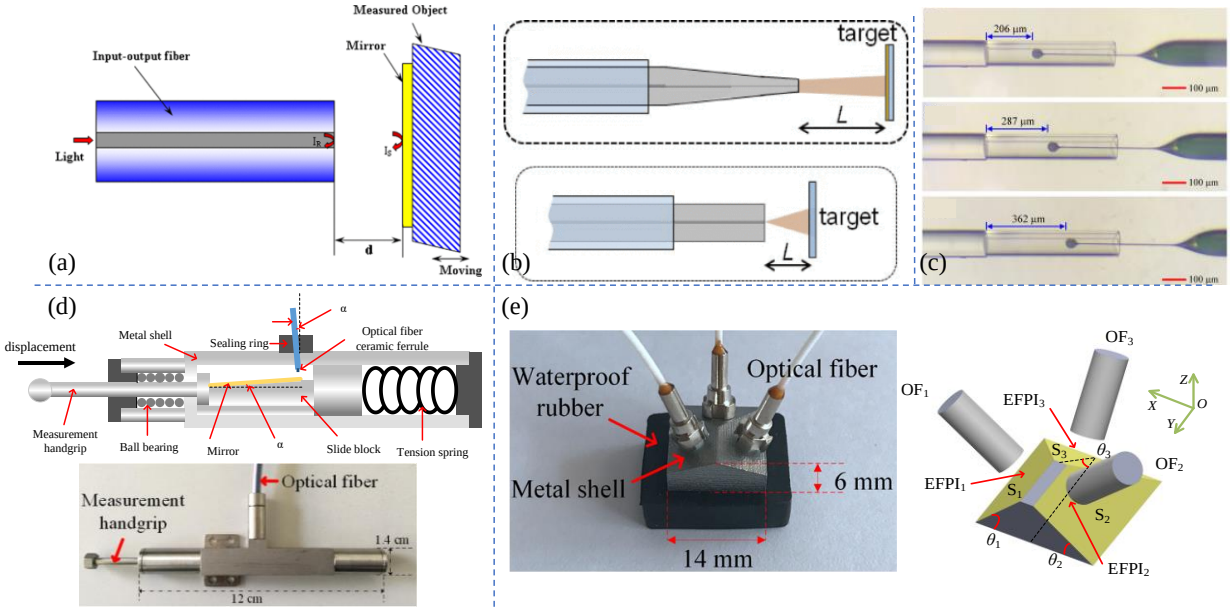

Fig. 3. EFPI-based displacement sensors. (a) A simple strategy of using an EFPI device as a displacement sensor by attaching its external mirror to the object under test [46]. (b) Using a tapered SMF to enhance the dynamic range of a conventional SMF-based EFPI device [47]. (c) Microsphere-based EFPI displacement sensor [48]. (d) Triangle geometry-based cm-range and sub-μm-resolution displacement sensor [49]. The protective metal shell and the measurement handgrip are made of Invar, and the length of the main part of the metal shell is about 12 cm. The cross-section of the rectangular part of the shell is 1.4×1.4 cm. The measurement handgrip is fully extended by 2.0 cm. (e) Three-dimensional displacement sensor based on the triangle geometry displacement transfer scheme [50]. The mirrors and endfaces of the corresponding optical fibers are parallel, such that three EFPIs are formed. The sensor is packaged and protected by a metal shell and a waterproof rubber casing. The size of the metal shell is 14 mm × 14 mm × 6 mm.

Fig. 3 shows a few examples of the EFPI-based displacement sensors reported in literature recently. The most straightforward way of using an EFPI device for constructing a displacement sensor is attaching its external reflector to an object of interest, whose movement consequently modifies the cavity length of the EFPI, as shown in Fig. 3(a) [46]. However, due to the divergence of the output light from the optical fiber end facet, the dynamic range of this EFPI displacement sensor was limited to a few mm. To address the dynamic range limitation, several strategies were proposed. Fig. 3(b) shows a side-by-side

comparison between a conventional single-mode fiber (SMF) based EFPI displacement sensor and a tapered SMF-based EFPI device. By scaling down the diameter of the core and cladding of the SMF, the divergence of the output beam of the tapered optical fiber tip was effectively reduced, thus enhancing the displacement measurement range to 80 mm [47]. Also, in addition to SMF, a strongly coupled multicore fiber (SCMCF) was spliced with an SMF to develop long-range displacement sensors (up to 50 mm) based on Fabry-Perot interference detection thanks to the enhanced light collecting capability introduced by the SCMCF [51]. Movable microspheres were employed to act as the second reflector of an EFPI device to develop compact high-sensitivity displacement sensors, as shown in Fig. 3(c) [48, 52]. Judicious mechanical designs were integrated with the EFPI device to develop more practical displacement sensors. A triangle-geometry displacement transfer mechanism was proposed and employed to develop a cm-range and sub-μm-resolution displacement sensor [49, 53]. A schematic and a photograph of the sensor are given in Fig. 3(d). It is worth mentioning that the design of the sensor is quite flexible where the dynamic range and sensitivity can be adjusted by simply varying the inclination angle of the mirror α (see Fig. 3(d)). Further extending the triangle geometry-based displacement transfer mechanism to a higher-dimensional space, a three-dimensional displacement sensor, as shown in Fig. 3(e), was developed and demonstrated for the characterization of interfacial sliding and debonding that is desired in structural health monitoring applications [50, 54]. A similar structure design was simplified as a two-dimensional sensor and was used to simultaneously measure the shrinkage and thermal expansion coefficient of mortar during its curing stage, showing the potential for practical applications [55].

Note that a conventional EFPI device is limited to measuring only the one-dimensional movement of its external reflector, i.e., out-of-plane displacement, which has hindered the development of EFPI sensors for a broader range of applications. Thus, additional efforts have been made in the development of delicate structures that can be used as the external reflector of EFPIs to construct sensors for potential multi-dimensional sensing. Examples include a metasurface, a step-structure reflector, and a three-dimensional integrated waveguide array, as shown in Fig. 4. By integrating an EFPI device with a plasmonic metasurface, a high-accuracy two-dimensional displacement sensor was demonstrated, where the out-of-plane displacement was quantified by variations of the Fabry-Perot interference pattern and the in-plane displacement was determined from the resonant wavelengths caused by the wavelength-selective metasurface resonators [56]. Using a step-shaped reflector (see Figs. 4(c) and 4(d)) to construct an EFPI device with dual Fabry-Perot cavities, two-dimensional displacement sensing was realized with the assistance of Fourier transform-based signal analysis [57, 58]. Further, by using a three-dimensional integrated waveguide array as the external reflector, a hybrid EFPI device was developed and demonstrated for three-dimensional positioning with the assistance of machine learning-based analysis [59]. However, the measurement precision and accuracy of the multi-dimensional sensor devices were sacrificed due to the complicated sensing spectra. More advanced demodulation techniques need to be investigated.

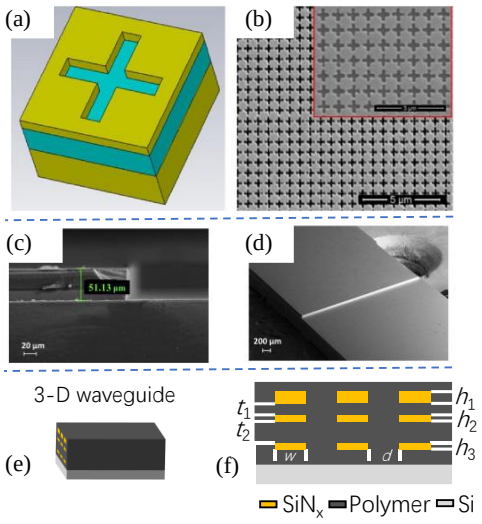

Fig. 4. Novel structures developed for constructing EFPI-based multi-dimensional displacement sensors. (a)-(b) Metasurface-based reflector [56]. (c)-(d) Step-shaped reflector [57]. (e)-(f) Three-dimensional integrated-waveguide array-based reflector [59].

2. Strain Sensors

Strain monitoring is of significant importance in structural health monitoring applications [60, 61]. FBGs are one of the most successful fiber-optic sensors that have been used in strain sensing applications due to their capability for large-capacity multiplexing [62, 63]. Meanwhile, the recent development of fully distributed fiber-optic strain sensors (DSSs) based on optical frequency domain reflectometry and optical time domain reflectometry has enabled many important applications that have been long desired in various fields [64, 65]. It seems that the research into EFPI-based strain sensors is not necessarily critical due to the technical readiness level of existing FBG and DSSs technologies. However, the EFPI strain sensors do provide unique aspects. For example, compared to FBGs, an EFPI device is smaller in gauge length, which is important for localized sensing. Also, the EFPI strain sensors generally have a much smaller temperature cross-talk effect due to the air-cavity. The measurement resolution of EFPI strain sensors is superior to DSSs and thus EFPI strain sensors are favorable where high-precision point sensing is needed. In this section, we discuss several represtative designs of EFPI strain sensors. It should be noted that there are a number of articles reporting the development of IFPI strain sensors [66, 67], which are out of the scope of this review.

One of the simplest methods to fabricate an EFPI device is inserting two cleaved optical fibers into a capillary tube, forming the so-called fiber-in-capillary structure, as shown in Fig. 1(b). Through judicious sensor packaging, an EFPI strain sensor based on the fiber-in-capillary structure was demonstrated simultaneously achieving a large dynamic range of up to 120000 $\mu\varepsilon$ (12%) and a high resolution of 10 $\mu\varepsilon$ [68]. Fig. 5(a) shows a schematic diagram of the strain sensor. The sensor configuration included three layers. Layer 1 is an SMF with a diameter of 125 μm; the intermediate layer (i.e., layer 2) is a capillary tube used to guide the two cleaved SMFs to move in parallel subject to tensile strains. The capillary tube has an inner diameter of 127 μm and an outer diameter of 350 μm. The outmost layer (i.e., layer 3) is a glass tube with an inner

diameter and outer diameter of 356 μm and 1000 μm. The glass tube is employed to improve the stability of the strain sensor. All the components are bonded using epoxy, as marked in the figure, and the sensor body is fixed to a thin metal sheet. Note that the intermediate layer (layer 2) was kept unbounded on the left side so that the fiber end facets can move freely in response to tensile strains. The fiber-in-capillary structure paved the way for the development of a number of air-bubble cavity-based strain sensors, and different strategies were proposed for sensitivity enhancement, e.g., increasing the active length of the cavity and reducing the sidewall thickness of the cavity, etc [69-72]. For example, as shown in Fig. 5(b), the Fabry-Perot cavity with a length of L_1 (i.e., the cavity where two-beam interference occurs) is sperate from the active cavity of the device with a length of L_2, forming the pillar-in-bubble structure [73]. The strain sensitivity of the device is amplified by a factor of approximately L_2/L_1; the larger the L_2-to-L_1 ratio, the higher the sensitivity. Using a such strategy, a miniature strain sensor with an ultra-low detection limit of 0.047 $\mu\varepsilon$ was demonstrated [74]. A mechanically-designed EFPI sensor with a resolution of 0.010 $\mu\varepsilon$ was developed based on the sensitivity amplification scheme mentioned above [75]. Furthermore, a cost-effective and embeddable EFPI strain sensor with a more practical packaging design was also reported, showing a resolution of 0.030 $\mu\varepsilon$ [76]. Fig. 5(c) shows a schematic diagram of the sensor structure and a photograph of a prototype device. Additionally, a buckled-beam structure was used to improve the measurement sensitivity of EFPI-based strain sensors, as shown in Fig. 5(d) [77]. The midpoint of the buckled beam would experience a vertical deflection when the device was subject to a horizontally compressive strain. Importantly, due to the buckled beam structure, the vertical displacement of the beam could be amplified by a factor of 6~17 compared to the displacement of the beam along the horizontal direction, indicating a strain sensitivity amplification factor of 6~17. The same strategy was also used to develop sensitivity-enhanced force and pressure sensors based on the EFPI principle, as shown later.

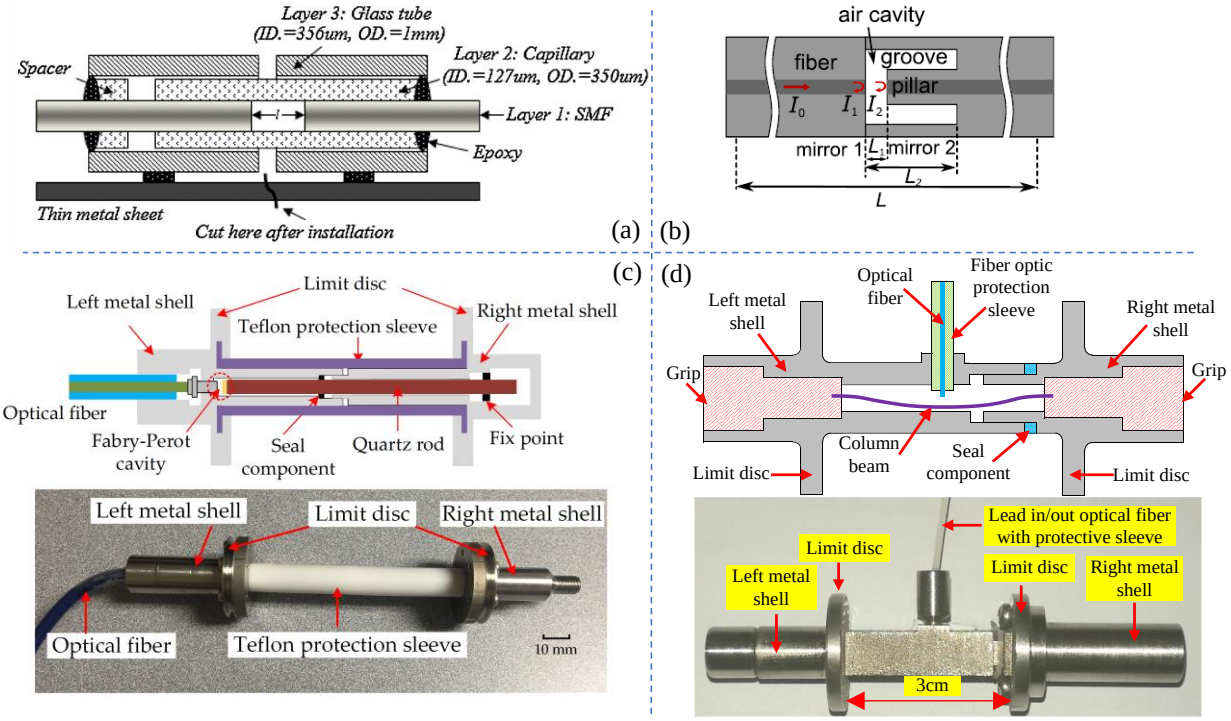

Fig. 5. EFPI-based strain sensors. (a) Fiber-in-capillary structure-based large-dynamic-range and high-resolution strain sensor [68]. (b) Pillar-in-bubble structure-based strain sensor with enhanced sensitivity [73]. (c) Schematic and photograph of the embeddable nano-strain sensor [76]. The principal part of the sensor consists of an optical fiber, a quartz rod with one end coated with a thin layer of gold, and two metal shells made of stainless steel. The length of the quartz is 10 cm, and the quartz rod was used due to its small coefficient of thermal expansion. The quartz rod was fixed to the metal shell at the fixed point, which is approximately 4 mm away from the right limit disc to achieve temperature compensation. (d) Schematic and photograph of the buckled beam-based strain sensor [77]. A buckled beam (length×width×height: 24mm×3mm×0.2mm) with a coated gold layer is pinned by two grips at both ends. An SMF is packaged in fiber ceramic ferrule and mounted inside the left metal shell through a drilled hole on top. The output SMF is fixed with a fiber-optic protection sleeve by a sealing ring. The mirror and the endface of the corresponding SMF are parallel, such that an EFPI is formed. The sensor is packaged with two metal shells. The initial distance between the limit discs on both metal shells is 3 cm.

3. Force Sensors

Precise measurements of axial/contact force are desired in various fields such as robotics, biomedical, and industrial applications [78-80]. Particularly, in biomedical applications, e.g., in magnetic resonance imaging, fiber-optic force sensors are especially advantageous due to their compact size, light weight, and immunity to electromagnetic interference [81-84]. Several ultra-sensitive force sensors have been developed based on the EFPI structure, as discussed below.

Inspired by the well-known fiber-in-capillary structure, a microfiber (MF) enabled EFPI device was demonstrated and used for high-sensitivity force sensing [85]. The sensor was constructed by fusion splicing a short section of MF between

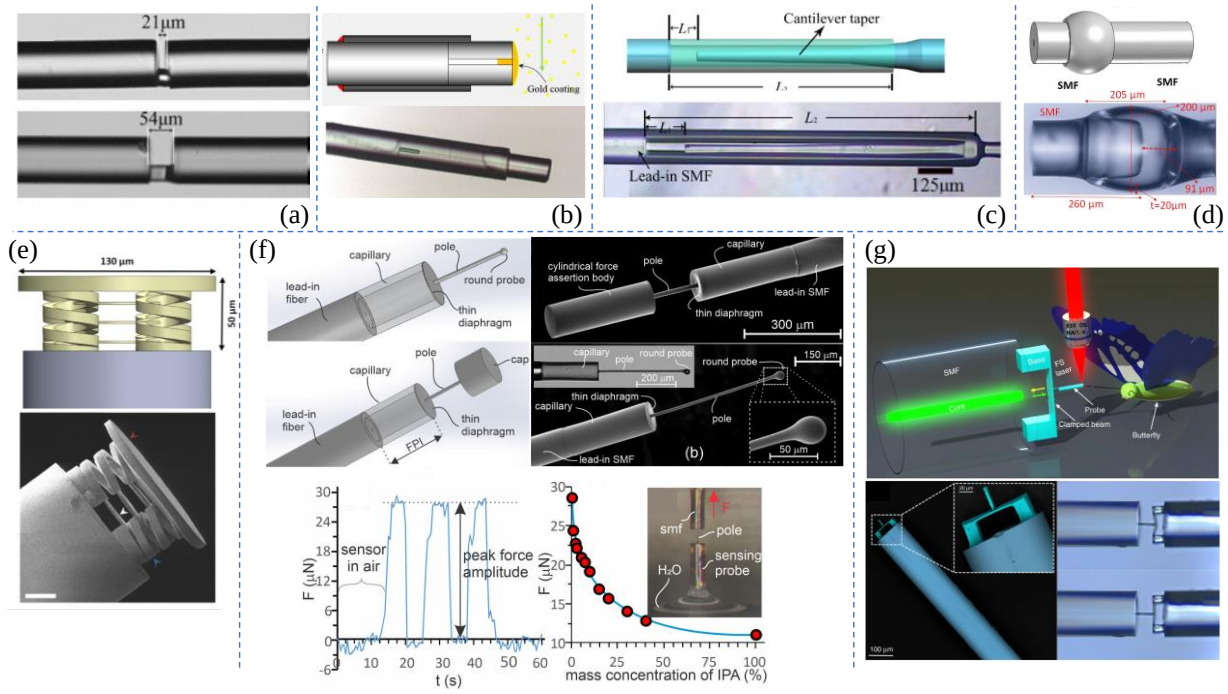

Fig. 6. EFPI-based force sensors. (a) MF-enabled force sensor [85]. Side-view microscope images of the EFPI sensors with different cavity lengths. (b) Air-liquid cavity-based force sensor [86]. Schematic and microscope image of the sensor. (c) Cantilever taper-plugged cavity force sensor [87]. Schematic and microscope images of the device. (d) Cleaved micro-air cavity-based force sensor [88]. (e) Fiber tip spring-structure-based force sensor [89]. Schematic and scanning electron microscopy (SEM) image of the force sensor. The optical fiber is shown in grey and the sensor in yellow. The tip of the optical fiber is visible in the bottom left corner. The white, blue, and red arrowheads respectively indicate the polymer plates that act as Fabry-Perot etalons for compression/force sensing, the springs that support the sensing plates, and the upper pad onto which forces are applied. Scale bar 25 μm. (f) Miniature all-fiber force sensor [90]. The top part shows the schematic diagrams and SEM images of sensors with rounded probe and cylindrical probe. Bottom part shows the demonstration experiment: Force measurement of the sensor retracted from distillated water as function of time; force measurement as a function of IPA mass concentration; and, sensor retracted from distilled water. (g) Fiber-tip polymer clamped-beam force sensor [91]. Schematic diagram and SME images of the sensor. The right bottom corner images are optical microscope images of the clamped-beam probe structure when pressed and released on the fiber-end surface.

two SMFs, as shown in Fig. 6(a). The diameter of the MF is much smaller than the SMFs such that the force sensitivity is considerably enhanced. Prototype devices with different diameters of MF and different cavity lengths were investigated. The 21 μm-long MF-enabled cavity with an MF diameter of 44 μm exhibited a force sensitivity of 167.4 nm/N, while the EFPI with a 56-μm MF (in diameter) and 127-μm cavity length showed a dynamic range of ~0.8 N, limited by the fragility introduced by the MF-beam configuration. An ultra-sensitive EFPI force sensor was reported with a sensitivity of 8700 nm/N based on a fiber-tip air-liquid-filled cavity [86]. The Fabry-Perot cavity was first partially filled with oil, and subsequently, a thin membrane of Parylene C was deposited on the outer surface of the oil to form a hermetically sealed hybrid cavity, as shown in Fig. 6(b). It is worth mentioning that measurements of insertion forces during experimental cochlear implantation were performed, demonstrating the high sensitivity of the sensor device. However, the hybrid cavity also brought high temperature measurement sensitivity to the sensor, which might cause confusion in practical applications. Simultaneous measurement of milli-Newton axial force and temperature based on a matrix calibration approach and a hybrid cavity was also reported [92]. Meanwhile, to overcome the fragility of the MF-based cavity and the temperature crosstalk of the air-liquid-based cavity, fiber-in-capillary-based air-gap EFPI forces sensors were developed with careful mechanical designs for sensitivity enhancement and temperature-crosstalk suppression. Using the sensitivity amplification scheme discussed in the section above (see Fig. 5(b)), a force sensor based on a cantilever taper-plugged EFPI device was reported, as illustrated in Fig. 6(c) [87], showing a force sensitivity of 841.59 nm/N and small temperature crosstalk as low as 0.011 nm/°C. A compact contact force sensor based on a micro-length SMF incorporated into a cleaved micro-air cavity was proposed, as shown in Fig. 6(d), achieving both a relatively high sensitivity of 14.2 nm/N and a large range of 10 N [88].

To further improve the sensitivity and resolution for force measurements, more sophisticated fabrication processes and structures were developed. The direct laser writing technique was used to create a force-sensitive spring structure on the tip of an optical fiber to construct a force sensor [89]. A schematic and a microscope image of the sensor are given in Fig. 6(e). The sensor consisted of three 1.5 μm-thick polymer plates suspended on an SMF tip with a plate-plate separation of 13 μm via four spring supporters. Multiple Fabry-Perot cavities are formed in the structure, resulting in a relatively convoluted interference pattern. The springs compress and bring the polymer plates together as the upper pad is subject to an external contact force. A singular value decomposition algorithm followed by linear regression or artificial neural networks was used to calibrate the complex response of the

sensor, and a measurement error of approximately 1.5 μN in a range of 0-50 μN was demonstrated. A miniature all-fiber force sensor with a resolution of 0.6 μN was then reported with a new structural design [90]. The sensor consists of two subassembly structures, i.e., the Fabry-Perot cavity and the pole-probe structure, as shown in Fig. 6(f). Specifically, the all-silica sensor includes a lead-in SMF, a short section of a thin-wall capillary, a thin flexible silica diaphragm, a silica post, and a rounded or cylindrical force sensing probe. Detailed fabrication processes can be found in [90]. The sensitivity of the sensor was optimized by considering a number of aspects. For example, the diameter of the pole directly affects the sensitivity of the sensor; the smaller the diameter, the larger the sensitivity. On the other hand, a reasonable radius of the pole is required to maintain the mechanical strength of the whole device. Also, the thickness of the diaphragm has to be precisely controlled to obtain the desired sensitivity. A miniature prototype device with a size not exceeding 800 μm in length and 125 μm in diameter exhibited a resolution of 0.6 μN in a range of 0.6 mN. A demonstration of the high sensitivity of the prototype device was performed by measuring the force when the sensor probe head was retracted from different liquids, as shown in Fig. 6(f). The peak force amplitude during the retraction is linearly proportionally related to the surface tension of a liquid; the larger the concentration of water-isopropyl alcohol (IPA), the large the peak force amplitude. With a more advanced micro-fabrication technique, a two-photon polymerization technique, a fiber-tip-polymer clamped-beam probe sensor was reported with a record-high resolution of 54.9 nN in a range of 2.9 mN [91]. A schematic diagram and SEM images of a prototype device are shown in Fig. 6(g), showing the elastic properties of the fiber-tip structure. The sensor exhibited an unprecedentedly low detection limit in direct contact mode and is comparable to that of an atomic force microscope. Other micro-cantilevers were also fabricated on the fiber top to form the so-called fiber-top sensors with high accuracy comparable to atomic force microscopes [93-95]. In addition to these miniature sensors, mechanically designed EFPI sensors with relatively large size were also reported. For example, the buckled beam structure was employed to develop a robust, embeddable, easy-to-manufacture, and high-sensitivity EFPI force sensor [96].

4. Tilt Sensors

Inclinometers or tilt sensors have attracted considerable research interest due to their potential applications in structural health monitoring and the study of solid Earth tides, etc [97]. A typical tilt sensor includes two parts, i.e., the tilt-sensitive element typically in the form of a pendulum, and the part that is employed to measure variations in tilt angles of the pendulum. In the case of EFPI-based tilt sensors, different types of pendulums including air bubble, liquid marble, and solid pendulum have been used.

Initially, a dynamic EFPI sensor based on a micro-air-bubble drifting in a liquid core fiber was explored for level sensing [98]. As the device is titled under different conditions, the position of the air-bubble changes, as illustrated in Fig. 7(a), resulting in a change in the Fabry-Perot cavity formed by the SMF-liquid interface and the adjacent liquid-air interface. Since an equilibrated state has to be reached, the air-bubble always stays at the two ends of the liquid microcavity when it is tilted. Therefore, the device cannot be used to measure the specific tilt angle. A tilt sensor based on a microbubble along an arc-shaped microcavity was then proposed to address this issue [99]. Schematics and microscope images of the sensor are given in Fig. 7(b). When the sensor is tilted, the air-microbubble will drift along the inwall of the ellipsoidal microcavity under three different types of forces, i.e., buoyancy (F), supporting force (N), and viscous resistance. The effect of these three forces on the microbubble is quite different in the case of the arc-shaped wall compared to the straight wall, which gives the ability of the sensor to measure the specific tilt angles. But the arc-shaped inwall limits the dynamic range of the sensor to -5° to 5° due to its working principle. Also, the repeatability and accuracy of the arc shape are quite challenging in the sensor fabrication stage. Therefore, a new approach based on the Marangoni effect was proposed to control the position of the microbubble suspended in ethanol to eliminate the effects from the inwall shape of the microcavity [100]. A 1550-nm laser source was used as a generator to produce a thermocapillary force. The combined effect from the thermocapillary force and buoyancy makes the microbubble suspend in the ethanol microcavity without contacting the inwall of the capillary. The suspending position of the microbubble varies when the sensor is tilted at a different angle, leading to a change in the Fabry-Perot cavity length formed between the interface of the lead-in fiber/liquid and the adjacent interface of the microbubble/liquid. An illustration of the laser on the position of the microbubble when the sensor is orientated at different directions is shown in Fig. 7(c). The prototype sensor achieved a dynamic range of -45° to 45°. In addition to the air-microbubble pendulum, liquid marble was also employed as the tilt-sensitive element in the development of EFPI tilt sensors. A mercury marble with a diameter of 1.3 mm and a length of 10 mm is dispensed into a hydrophobic agent-processed capillary tube, serving simultaneously as the liquid pendulum and the external reflector of an EFPI device, as shown in Fig. 7(d) [101]. A large dynamic range of -90°-90° was achieved.

Both the air and liquid pendulum-based tilt sensors showed limited resolution (~0.017° [101]). High-sensitivity solid pendulum tilt sensors were then developed based on the EFPI principle, taking advantage of the capability of the EFPI principle for resolving subtle changes in the cavity length (i.e., movement of the solid pendulum) [102-105]. Using a two-rope suspended rectangular mass block as the tilt responsive element to construct an EFPI device, a tilt sensor with 20 nrad resolution was demonstrated [106], as shown in Fig. 7(e). When the sensor is tilted at an angle $\Delta\theta$, the supporting rod will be tilted at the same angle duo to the rigid connection. Meanwhile, the two supporting ropes will remain perpendicular to the horizontal direction confined by the gravitational field. As a result, the tilt of the sensor results in a length change in the Fabry-Perot cavity formed between the optical fiber endface and the adjacent endface of the mass block. Importantly, due to the two-rope configuration forming a parallelogram, the two reflecting surfaces of the EFPI device remain parallel during operation, such that the dynamic range of the sensor is ensured. Also, a cross paddle is integrated into the sensor design to increase the stability of the device by physically reducing oscillations from environment-induced vibrations. The prototype device realized

a resolution of up to 20 nrad, which makes the sensor capable of sensing three-dimensional space with the assistance of machine learning-based signal analyses [107-109]. Extending the design into a two-dimensional space, a two-dimensional high-sensitivity tilt sensor was then developed, capable of simultaneously measuring tilt angles in two orthogonal dimensions [110]. Schematic, perspective view of the assembly figure, photograph of a prototype device, and an illustration of the implementation of the device for structural health monitoring of a gravity dam are given in Fig. 7(f). These rope-suspended pendulum-based tilt sensors were developed for static tilt sensing, while a vertical cantilever-suspended solid pendulum structure was developed to construct a high-resolution dynamic tilt sensor [111], suitable for the measurement of inclination in vibrating environments involved in structural health monitoring applications.

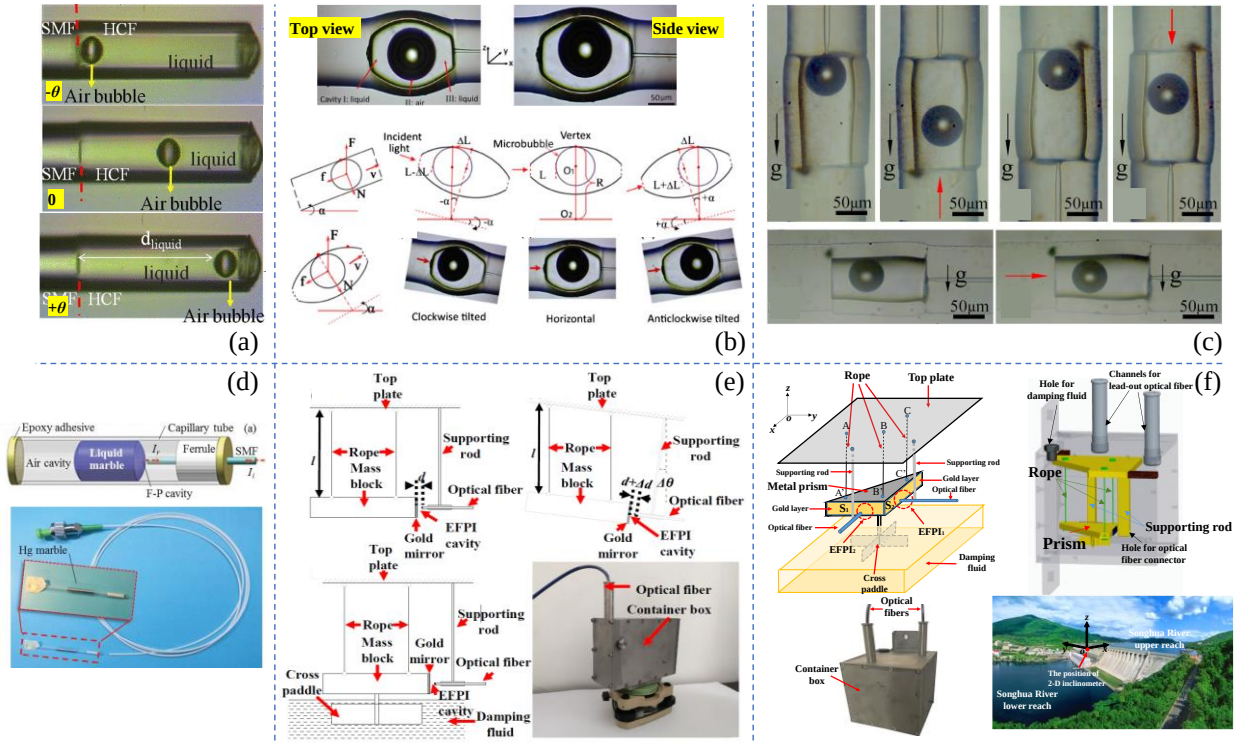

Fig. 7. EFPI-based tilt sensors. (a) Air-bubble drifting in a liquid core fiber-based level sensor [98]. Microscope images show the evolution of the air bubble as the device tilted from a negative angle (-θ) to a positive angle (+θ). (b) Air-bubble drifting in an air-shaped microcavity-based tilt sensor [99]. The top part shows microscope images of the tilt sensors in the top view and side view. The bottom part shows the free-body diagrams of the dynamic microbubble drifting along the straight inwall and arc-shaped inwall and schematic diagrams and the microscope images of the sensor in different tilt states. (c) Laser-suspended microbubble-based tilt sensor [100]. Illustrations of the effects of the laser on the suspension position of the air-microbubble when the sensor is orientated at different directions. The red arrows indicate the directions of the light source, and the black arrows indicate the gravity direction. (d) Liquid marble-based tilt sensor [101]. (e) High-resolution solid-pendulum-based tilt sensor [106]. Schematic diagrams and photograph of the sensor tilted at different angles (0° and $\Delta\theta$). The inclinometer is packaged in a box made of Invar to reduce the temperature cross-sensitivity. (f) High-resolution solid-pendulum-based two-dimensional tilt sensor [110]. Schematic diagram, perspective view of the assembly figure, and photograph of a prototype device. The figure in the right bottom corner shows a photograph of the Fengman Dam where the prototype sensor was mounted for the long-term (one-year) monitoring of its tilt angles under operation.

5. Acceleration and Vibration Sensors

Accelerometers are widely used in seismic monitoring, oil exploration, and health monitoring of various infrastructures, mechanical machines, etc [112]. The development of fiber-optic accelerometers has gained wide interest because of their inherent advantages such as high sensitivity and immunity to electromagnetic interference [113]. This section reviews specifically the recent progress of EFPI-based acceleration and vibration sensors. The EFPI configuration is an ideal candidate for constructing accelerometers as it can easily be configured within a reflective probe with miniature size and for its capability for resolving sub-nanometer scale movement of its external reflector that can be designed as a vibration-sensitive element.

The most straightforward method to develop a vibration system is to attach the external reflector to the measured object of interest, where the vibration directly changes the cavity length of the EFPI device [104, 114]. Assisted with the laser emission frequency modulated phase generated carrier (PGC) demodulation scheme, non-contact, dynamic, and high-resolution measurement of vibration was achieved [114]. However, this type of vibration sensor is not compact. A typical compact EFPI-based accelerometer includes five elements, i.e., a fiber tip used to input probing light, a reflector used to act as the external mirror to form the Fabry-Perot cavity, a spring as an elastic element, a mass as the inertial element, and a packaging columnar shell. A lot of efforts have been made in the optimization of the material and structural design of the spring which fundamentally predicates the resonance frequency and responsivity of the accelerometer [115-119]. One of the most widely used diaphragm structures is the circular mesh spring configuration, as illustrated in Fig. 8(a). When an external acceleration is exerted perpendicular to the mesh spring, a deformation of the mesh occurs. A silicon

micro-mirror is attached to the center of the mass to facilitate the formation of the Fabry-Perot interference cavity. A piezoelectric oscillator is used to modulate the cavity length at an audio frequency to employ the PGC demodulation scheme. Three acceleration probes are arranged perpendicularly to one another to minimize the off-axis crosstalk, as shown in Fig. 8(a). Both the mesh spring and the mass are made of stainless steel using a computerized engraving machine. The prototype device demonstrated an acceleration resolution of 48 ng/Hz$^{1/2}$ with a resonance frequency of 160 Hz below which the responsivity reached 36 dB re 1rad/g [115]. Note that the responsivity and resonance frequency can be tuned by adjusting the structural parameters of the mesh spring including the width, thickness, and turns. The susceptibility of the spring to sidewise accelerations must be taken into account, representing a tradeoff that has to be evaluated during the spring design [115]. The same structure was fabricated on a silicon wafer using the micromachining process, showing the potential for mass production of miniature all-optical accelerometers [117], shown in Fig. 8(b). Both the mesh spring structure and the demodulation scheme were improved to enable a sensor with high resolution, high dynamic range, high speed, and absolute measurement capability [116]. The prototype device was validated by simultaneously recording both low- and high-frequency acceleration components in an elevator system during operation.

In addition to the mesh spring structure, a thin diaphragm is used as the elastic element to develop accelerometers [120]. Fig. 8(c) shows a side-by-side structural comparison between a traditional diaphragm-based accelerometer and one with an improved design [121]. In a traditional sensor device, all the components are assembled into the packaging shell separately and individually, indicating unavoidable mechanical errors in the sensor assembly. To overcome the inconsistency, a diaphragm-mass-collimator integrated structure was proposed, showing a more compact structure and more controllable manufacturing process with high consistency. Different materials, such as aluminum-polyimide composite [122] and polyethylene [123], were explored as the material of the diaphragm for performance enhancement. The fiber-top cantilever was also used as the elastic element to develop EFPI-based accelerometers [124]. An X-shaped glass cantilever beam was fixed to the sensor body to construct an EFPI accelerometer, as shown in Fig. 8(d) [125]. Driven by the specific application in seismic detection, the structural design of the cantilever beam was optimized. The sensor accurately sensed and registered the ground acceleration associated with the earthquakes that occurred in Central Italy in November 2016. The structure of the cantilever-based elastic element was further investigated recently, where a simple cantilever and a specially-designed membrane sustained by four cantilevers were thoroughly studied [126]. Both of the lab-on-fiber accelerometers showed competitive performance to commercial ones, demonstrating the potential and the versatility underlying the integration of micro-opto-mechanical structures with fiber-optic sensing technologies towards a new generation of lab-on-fiber accelerometers. A high-sensitivity and wide-dynamic range over 10 kHz accelerometer was also reported based on a side test-mass configuration, as shown in Fig. 8(e) [127, 128]. One of the devices combined a monolithic fused-silica oscillator and a high-finesse Fabry-Perot micro-cavity with a quality factor of 3.5×10^5, capable of reaching a resolution higher than 100 ng/Hz$^{1/2}$ over 10 kHz. In addition to the proof mass serving as the inertial element, the fiber itself was also explored as the vibration-sensitive element, from which miniaturized all-fiber vibration and acceleration sensors were successfully developed [129, 130].

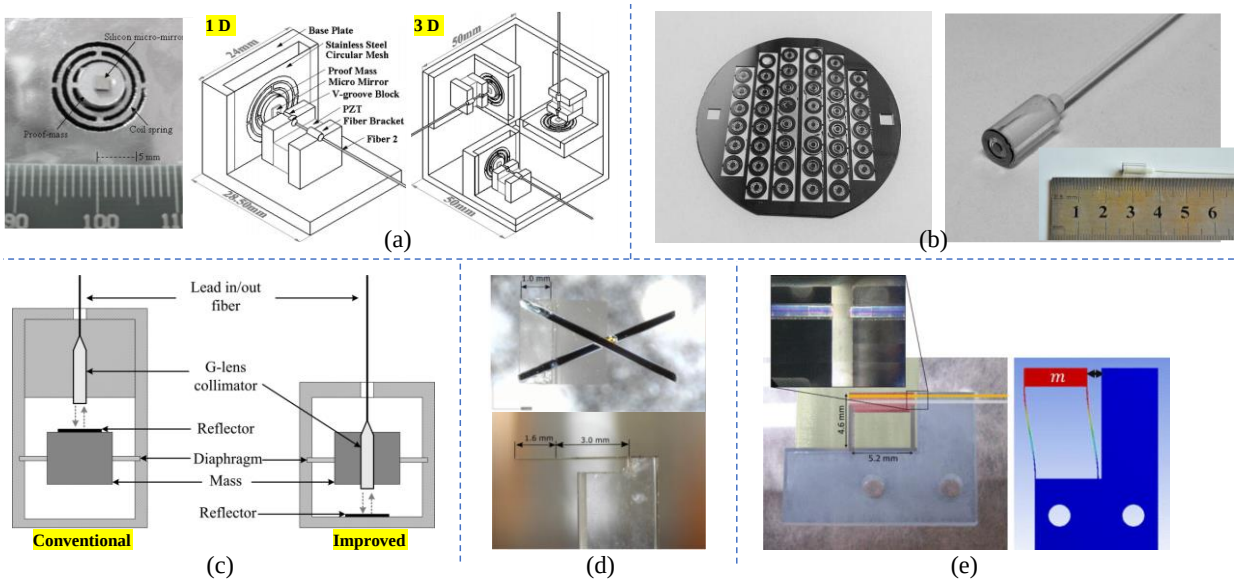

Fig. 8. EFPI-based acceleration and vibration sensors. (a) Three-dimensional high-resolution accelerometer [115]. Photograph of the mesh spring fabricated on a 100-μm thick stainless steel film and a silicon micro-mirror fixed to the center; schematics of the one-dimensional acceleration probe and three-dimensional acceleration sensing module. (b) All-optical accelerometer [117]. Photographs of the mesh-spring-based elastic element on a single silicon wafer and fabricated miniature all-optical sensor. (c) Diaphragm-based accelerometer. Side-by-side comparison between a traditional sensor and one with an improved design [121]. (d) X-shaped glass cantilever-based accelerometer [125]. Front view and side view of the seismic accelerometer. (e) Side test-mass based accelerometer [127]. Photograph and sketch of the monolithic fused-silica mechanical oscillator with the integrated fiber micro-cavity (magnified in the upper left corner).

6. Pressure Sensors

Fiber-optic tip EFPIs are one of the best candidates for the measurement of pressure variations due to their miniature size, capabilities for remote operation, resistance to corrosion, and harsh-environment survivability [131-138]. The construction of an EFPI-based pressure sensor typically involves the bonding of a thin diaphragm to an optical fiber with a cleaved end facet, forming a hermetically sealed Fabry-Perot cavity. The optical fiber endface and the diaphragm serve as the two reflectors of the cavity. The diaphragm deflects when the external pressure changes, leading to a change in the effective cavity length of the Fabry-Perot cavity. In such a context, the external pressure is encoded into the interference signal of the EFPI. In general, the development of EFPI-based pressure sensors has evolved along two different paths, where one focuses on measurement sensitivity and the other is dedicated to harsh-environment (e.g., high temperatures) compatibility. In this section, these two different types of EFPI pressure sensors are reviewed in detail. Note that an additional strategy for sensing gas pressure based on monitoring changes in the refractive index is out of the scope of this article [139-142].

Among a variety of factors that determine the pressure measurement sensitivity of EFPI sensors are the characteristics of the diaphragm, such as material property, thickness, effective diameter, etc. Conventional materials such as silica are often used as the diaphragm due to their good stability and similar thermal expansion coefficient to an optical fiber [143-145]. However, the fabrication of an ultra-thin (e.g., sub-micron scale) silica diaphragm is complicated and challenging, thus limiting the highest sensitivity that can be realized by silica-diaphragm-based EFPI pressure sensors. It is worth mentioning that with the advancement of micromachining techniques, nanothick silica diaphragms, up to 320 nm [146] and 170 nm [147], were successfully fabricated on the fiber tip for highly sensitive pressure sensing, as shown later. In comparison with silica, polymer materials are much easier to process and have been employed as the elastic diaphragm element for EFPI pressure sensors. For example, two different polymer materials with different elastic properties, i.e., polyurethane and polystyrene, were investigated as the diaphragm material in a previous study [148], showing a pressure resolution up to 10 Pa. However, due to the porous cellular structure of the polymer, the sensor must be stabilized before use. Other materials were then explored as the elastic diaphragm, such as a nanothick silver diaphragm [149], a sub-nanometer graphene diaphragm [150], a silk fibroin diaphragm [151], PDMS diaphragms [152-154], silicone rubber [155], and an epoxy adhesive film [156], a metal diaphragm [157, 158], etc. A detailed comparison between these EFPI pressure sensors is given in Table I. Note that in addition to fusion splicing a hollow core fiber to a cleaved optical fiber to form the cavity, other methods including wet etching a spliced multimode fiber [148], 3D μ-printing [159], and focused-ion-beam micromachining [160] were also explored. It is interesting that by combining the EFPI principle with conventional mechanical structures, high-performance yet low-cost pressure sensors (only involving standard mechanical welding and cutting processes in sensor construction) were successfully developed. For example, using a buckled beam structure to amplify the pressure-induced deflection of a metal diaphragm, a sensor with high sensitivity of 169 nm/kPa (cavity length change/pressure change) in a pressure range of 1000 kPa was reported, as shown in Fig. 9(a) [157]. Using an EFPI to read the pressure-induced displacement of a C-shaped Bourdon tube, as shown in Fig. 9(b), an ultra-high resolution of 0.1 Pa was realized [161]. Acoustic pressure sensing was also demonstrated using such a simple configuration due to its ultra-high sensitivity up to 23500 nm/kPa (cavity length change/pressure change).

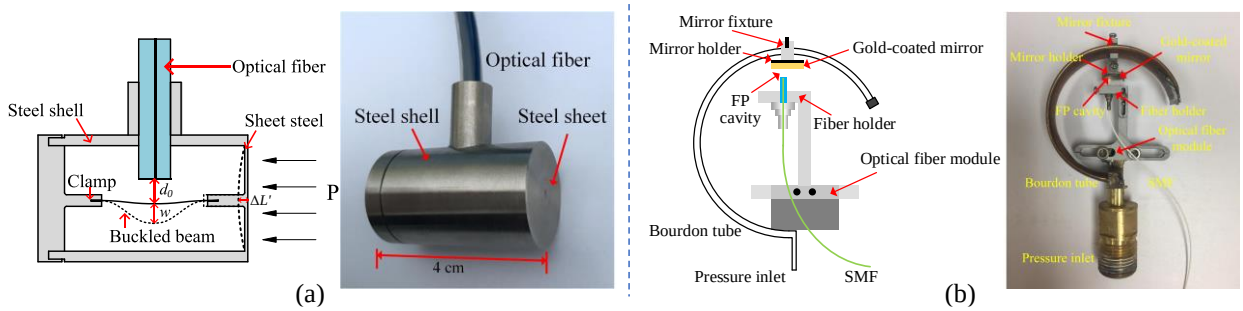

Fig. 9. Conventional mechanical structure-assisted high-sensitivity EFPI pressure sensors. (a) Schematic and photograph of the buckled beam-amplified metal diaphragm-based pressure sensor [157]. (b) Schematic and photograph of the C-shaped Bourdon tube-based pressure sensor [161].

The above-mentioned EFPI sensors are not suitable for pressure sensing at elevated temperatures because of the poor thermal stability of these diaphragms. Meanwhile, the large thermal expansion coefficient mismatch between the diaphragm and the cavity (typically silica) will cause severe stress in the sensor fabrication, which will degrade the sensor and ultimately lead to a crack in the diaphragm when it comes to high-temperature environments [162]. Thus, a diaphragm made of high-temperature stable material such as silica is desired in the development of pressure sensors for high-temperature applications [144]. Moreover, the bonding between the diaphragm and the cavity should avoid the use of polymer adhesive [163, 164]. In such a context, the so-called all-silica EFPI pressure sensor was reported in [162], which allowed high-temperature operation up to 700°C. Fig. 10(a) gives a schematic diagram of the all-silica pressure sensor. The bonding between the SMF and the ferrule as well as between the diaphragm and the cavity is realized by a CO_2 laser thermal fusion method. A small section of multimode fiber was spliced to the SMF to minimize the temperature cross-sensitivity of the pressure sensor [162, 165]. Instead of using a ferrule, all-fiber

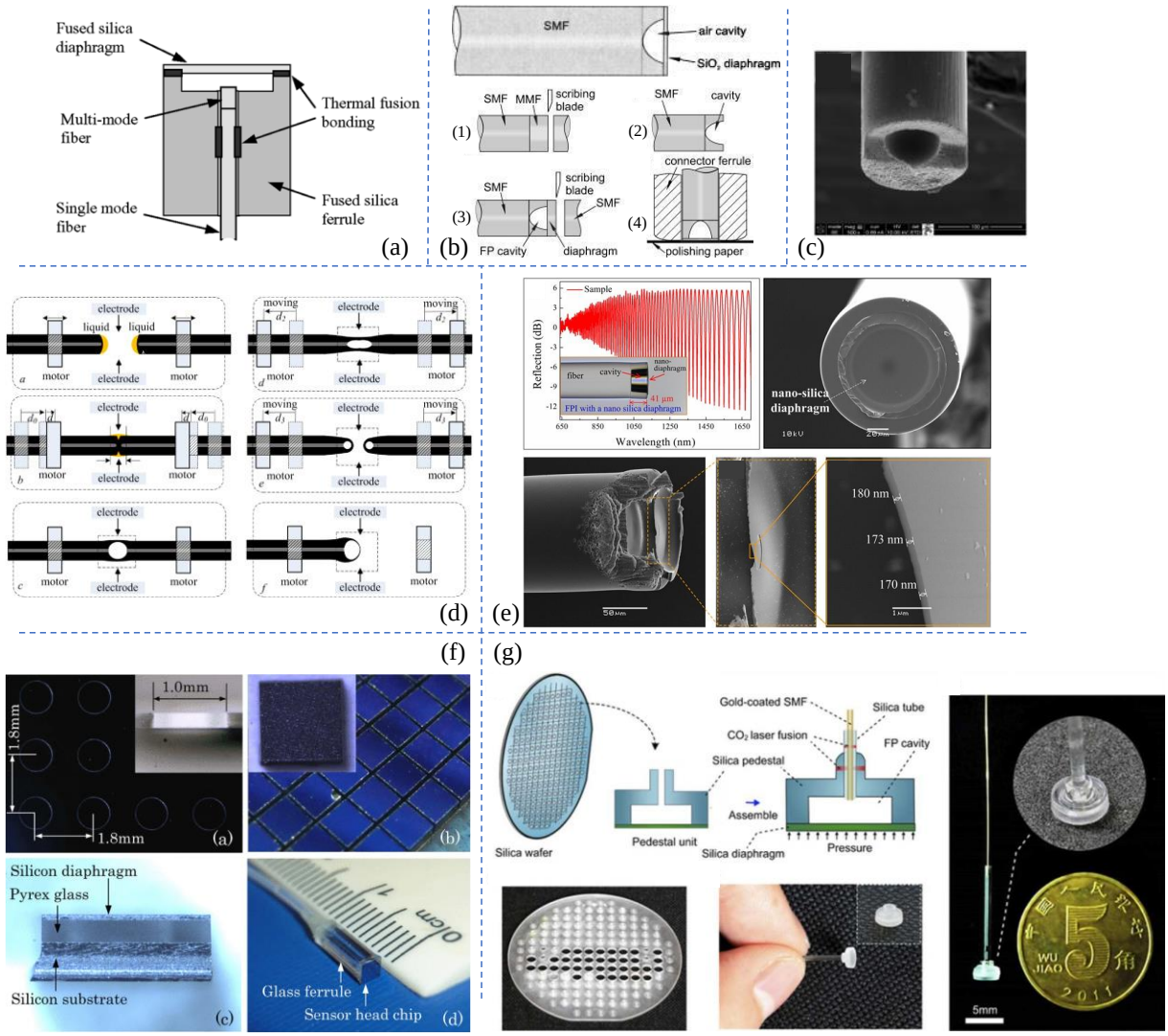

Fig. 10. EFPI pressure sensors. (a) Temperature-insensitive pressure sensor [162]. (b) All-fiber miniature pressure sensor [143]. (c) Fs-laser micromachined pressure sensor [166]. (d) Multi-step fabrication process based on an improved arc discharge technique for obtaining a nanothick silica diaphragm [146]. (e) Nanothick silica diaphragm-based EFPI pressure sensor [147]. (f) The first reported batch-producible EFPI pressure sensor with temperature self-compensation [167]. (g) High-temperature batch-producible EFPI pressure sensor [168].

miniature EFPI pressure sensors with a diameter of 125 μm (i.e., the diameter of SMF) were also demonstrated [143, 169, 170]. Fabrication of the all-fiber sensor typically involves a few steps (see Fig. 10(b)): (1) A section of MMF is spliced to a lead-in SMF, and the MMF was cleaved to retain the desired length connected to the SMF. (2) The SMF-MMF structure is etched in hydrofluoric (HF) acid for a certain time. Because the germanium-doped MMF silica core will be etched much faster than the undoped region, a cavity is formed at the end of the SMF. A buffer layer (e.g., pure silica-core MMF) can be inserted in-between the SMF-MMF to prevent the SMF from being etched by the HF [169]. The MMF can also be replaced with custom-designed fiber with higher dopant concentration for faster and more controllable wet etching [171]. The first two steps can be replaced by splicing and precision cleaving a section of hollow core fiber to the lead-in SMF [172, 173]. (3) Another section of the fiber is spliced to the SMF with the cavity on its end to realize a hermetic seal and also a Fabry-Perot cavity. This additional fiber is then cleaved with a residual length (e.g., 10-50 μm) serving as the diaphragm responsive to pressure variations. (4) The diaphragm is then polished for the reduction of its thickness. The final thickness of the diaphragm is typically a few micrometers (e.g., 3-5 μm), which is too thick to provide high sensitivity, but is suitable for high-pressure measurements (e.g., 30 MPa) [172]. Additional processes can be employed to fine tune the silica diaphragm thickness via wet HF etching [143]. Instead of using a spliced and cleaved fiber as the diaphragm, a commercial silicon wafer with a thermal oxide layer was investigated to obtain a uniform and thin silica diaphragm [145]. Femtosecond laser micromachining was also employed to create an in-fiber micro-cavity and reduce the thickness of the associated silica diaphragm [166], as shown in Fig. 10(c). The micro-cavity with a length of ~8 μm provided the sensor with a low temperature cross-sensitivity. The roughened outer surface of the diaphragm provided the sensor with a clean spectrum without any amplitude modulation, making it insensitive to environmental conditions. Custom-designed and improved arc discharge technique were explored to fabricate nanothick silica diaphragms on the tip of optical fiber [146, 147, 174, 175]. A

multi-step fabrication process of a nanothick-diaphragm pressure sensor is given in Fig. 10(d), which is simple and cost-effective. A nanothick silica diaphragm with a thickness of ~170 nm was resulted, as shown in Fig. 10(e), based on the arc discharge technique. In addition to silica, other stable materials such as alumina ceramic [176], sapphire [177], magnesium oxide [178], were employed as the diaphragm material. However, the major challenge for these pressure sensor is the low repeatability and manufacturing throughput and therefore is not suitable for batch production. In recent years, researchers have been combining the EFPI principle with microelectromechanical systems (MEMS) fabrication techniques to develop batch-producible EFPI pressure sensors [167, 168, 179-182]. In [167], a silicon-glass-silicon sandwich structure was produced by double-sided anodic bonding of a through-holes-array-structured Pyrex glass wafer and two silicon wafers, as shown in Fig. 10(f). Each of the element could be bonded to an SMF using a thin layer of adhesive for constructing a pressure sensor with capability of simultaneously sensing temperature variations. To improve the thermal stability, laser fusion was employed to fix the chip element to the lead-in SMF for high-temperature applications, as shown in Fig. 10(g). Very recently, the same group reported batch-producible all-silica EFPI pressure sensors using silica wafer, pushing the temperature tolerance up to 800°C [168].

Table I. Comparison of various EFPI pressure sensors.

Sensor configuration and material	Fabrication method	Size (μm): cavity length diaphragm thickness	Sensitivity[a] (nm/kPa)	Pressure range (kPa)	Resolution (Pa)	Temperature limit (°C)
Bare fiber + polymer diaphragm [148]	Splicing, wet etching, dip coating	55-60 4	NA	40/1200	10	NA
Ferrule + nanothick silver diaphragm [149]	Mechanical assembly, electroless plating	290 0.13	70.5*	50	NA	80
Ferrule + graphene layer [150]	Splicing, mechanical assembly, film transfer	21 0.00071	39.4*	5	NA	NA
Ferrule + silk fibroin diaphragm [151]	Mechanical assembly, film transfer	80 20	12.3*	80	NA	NA
Ferrule + hybrid PDMS diaphragm [152]	Mechanical assembly, MEMS processing, adhesive	~912 NA	1410*	4	30	NA
Capillary + silicone rubber [155]	Mechanical assembly, adhesive, spin coating	58 ~250	0.68**	50	NA	60
Capillary + epoxy film [156]	Mechanical assembly, adhesive	30 8.74	0.26**	70	87	NA
Bare fiber + SU-8 diaphragm [159]	3D μ-printing	91 11	0.0029**	700	NA	65
Ferrule + metal diaphragm + buckled beam amplification [157]	Mechanical assembly	200 800	169*	1000	5.2	60
Ferrule + Bourdon tube [161]	Mechanical assembly	192 NA	23500*	40	0.1	NA
Ferrule + silica diaphragm [162]	Mechanical assembly, laser thermal bonding	38.9 NA	0.425*	1378	68.9	700
Bare fiber + silica diaphragm [143]	Splicing, wet etching, polishing	40 NA	3.4*	40/1000	300	NA
Bare fiber + silica diaphragm [145]	Splicing, wet etching, thermal bonding	NA 0.75	11*	140	NA	NA
Bare fiber + silica diaphragm [166]	Splicing, arc fusion, fs laser micromachining	8 2.5	0.28*	689.5	180	700
Bare fiber + silica diaphragm [146]	Splicing, arc fusion	NA 0.5	1.036**	2000	NA	100
Ferrule + sapphire diaphragm [177]	Mechanical assembly, thermal bonding	180 420	NA	700	NA	800
Ferrule + silicon diaphragm [167]	MEMS, adhesive	200 25	12.82*	250	NA	70
Ferrule + silicon diaphragm [179]	MEMS, laser thermal fusion	140 95	8.5*	500	122	350

Ferrule + silica diaphragm [168]	MEMS, laser thermal fusion	170 200	3.54*	1000	NA	800

[a]The symbol * represents “cavity length change/pressure change” and the symbol ** denotes “wavelength shift/pressure change”. NA, not available.

7. Acoustic and Photoacoustic Sensors

Acoustic is an important carrier of information. Acoustic detection has been applied to many occasions, such as hydrophone instrumentation, earthquake forecasting, explosion monitoring, and so on. Compared with the sensors based on piezoelectricity, sensors based on optical fiber have the merits of small volume, high sensitivity, low cost, etc. This section reviews EFPI-based acoustic sensors, which mainly refer to infrasound detection sensors and their application in photoacoustic detection. The common configuration of a fiber-optic acoustic sensor involves a flat optical fiber end face with an acoustic responsive element, e.g., a thin diaphragm or a cantilever.

The diaphragm-type EFPI sensor utilizes the characteristic that vibration will introduce pressure on the diaphragm and therefore leads to a deflection of the diaphragm. It can be divided into three categories according to the diaphragm material, i.e., polymer-based, metal-based, and 2D material-based. The Young's modulus of polymer is much smaller than metal, which makes the polymer diaphragm-based sensor have a more sensitive acoustic response. A composite diaphragm which is composed of a small round aluminum foil and a polymer film was proposed in [183]. Fig. 11(a) presents the sensor structure. The round aluminum foil plays the role of a reflective mirror. The acoustic sensitivity can be up to 121 mV/Pa. After that, a sensitivity-enhancing method was proposed, where the two EFPI structures utilize the same composite diaphragm [184], as schematically shown in Fig. 11(b). This structure configuration forms a Michelson interferometer, which doubles the acoustic detection sensitivity. The Parylene-C diaphragm can be made very thin to obtain a higher sensitive response [185]. The pressure sensitivity can be up to 2239 nm/Pa. The large Young's modulus of metal makes it hard to realize higher sensitive acoustic sensing. To get a more sensitive response, the thickness of the metal film should be largely reduced. The silver mirror reaction [149, 186] and electron beam evaporation [187] are employed to prepare thin metal films. Besides, the corrugated silver diaphragm is also bonded to the optical fiber probe to increase the sensitivity [188]. The sensing structure is given in Fig. 11(c), and the sensitivity reached up to 82.65 nm/Pa. The 2D material possesses the merits of thin thickness and good mechanical properties. The graphene diaphragm-based EFPI sensor can realize a wide band frequency response up to 20 kHz [189, 190]. The schematic graph of graphene diaphragm based EFPI is shown in Fig. 11(d). The MEMS fabrication process is also adopted to fabricate the acoustic sensor [191, 192], which is presented in Fig. 11(e). It can achieve a tight bond of diaphragm and avoid unexpected and detrimental influence on the film during the diaphragm transfer progress. Fig. 11(f) presents another MEMS fabrication scheme, which fabricates a cantilever on the silicon-based diaphragm. It can detect weak acoustic since the free end of the cantilever is not restricted [193]. The sensitivity of acoustic pressure reached 1.753 μm/Pa at 1 kHz.

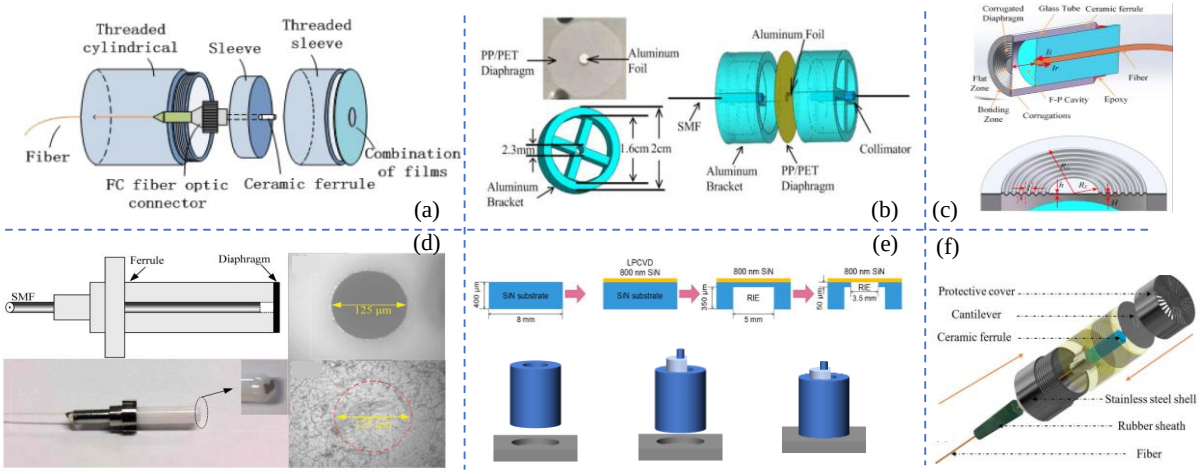

Fig. 11. EFPI-based acoustic sensors. (a) A composite film-based acoustic sensor [183]. (b) A differential principle-based sensor [184], including a microscope image of the diaphragm, the schematic of the Aluminum bracket, and the assembly structure. (c) A corrugated diaphragm-based sensor [188]. (d) A graphene diaphragm-based sensor [190]. (e) Acoustic sensor fabricated based on the MEMS technique [191]. (f) MEMS process-based acoustic sensor [194].

Photoacoustic spectroscopy is a typical application of acoustic sensors. Different gases have their unique absorbing spectroscopy. The gas in the cavity exhibits local thermal expansion after absorbing light energy, and generates mechanical waves. The amplitude of a mechanical wave is relevant to the concentration of the gas. The photoacoustic spectroscopy of gas can be obtained by scanning the excitation source. The typical acoustic sensor is a cantilever-based optical fiber EFPI, which is shown in Fig. 12(a) [195, 196]. The photoacoustic spectroscopy detection system is shown on the right of Fig. 12(a). The cantilever is located at the center of the diaphragm, and the acoustic sensor is positioned in the radial direction of the photoacoustic cell. The excitation laser is injected into the photoacoustic cell axially, and the acoustic will be generated after the gas absorbs the energy of the light. The acoustic measurement is achieved since the output voltage of the photodetector is proportional to the vibrating acoustic pressure, and it achieves

a C_2H_2 concentration detection sensitivity of 2.281 mV/ppm. A photoacoustic gas sensing scheme with high sensitivity is proposed based on a differential method, and the sensing structure is presented in Fig. 12(b) [195]. The sensing structure is composed of two absorbing cells. The cell without excitation light plays a role in background noise elimination. The minimum detection limit can reach 0.6 ppb, and the normalized noise equivalent absorption coefficient is 1.79×10^{-10} $cm^{-1}W/Hz^{1/2}$. To accelerate the gas exchange speed and reduce the volume of the sensor, the excitation light and the detection light are arranged in parallel mode, which is shown in Fig. 12(d) [197]. After that, a photoacoustic sensing structure with a more compact structure was designed, whose gas cell is about 1.7 μL in volume. The sensing probe is shown in Fig. 12(c) [198], where the probe is equipped with a cantilever and a channel. What's more, the excitation light and sensing light can be multiplexed in the same channel by a wavelength division multiplexer. Fig. 12(e) presents a simple sensing structure for gas concentration detection [199]. The thin silver film endows the sensor with low temperature cross-sensitivity, high detection resolution, and a large sensing range. Besides, thermoacoustic spectroscopy based on a quartz tuning fork is also applied to gas concentration detection. The sensing principle is different from photoacoustic sensing since the light attenuation in gas rather than the acoustic generated by the gas is concerned in this scheme [200]. The schematic diagram of a compact sensing probe is shown in Fig. 12(f) [201], and the minimum detection limit of H_2S can reach 422 ppb.

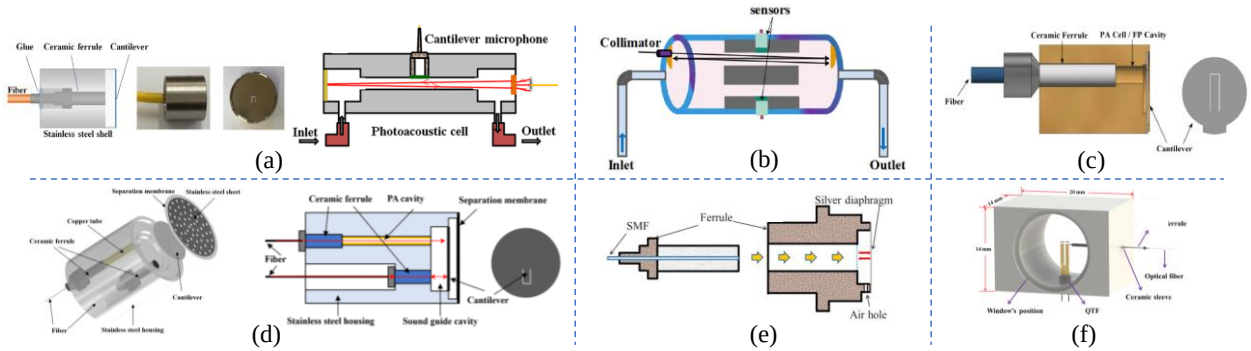

Fig. 12. EFPI-based photoacoustic gas sensors. (a) The structure configuration of the sensor with separate excitation and detection light sources [193]. (b) The structure configuration of the photoacoustic sensor based on differential detection [195]. (c) The structure configuration of the sensor probe multiplexing the excitation and probe light [198]. (d) The sensing probe with coaxial structure [197]. (e) The sensing probe with a silver diaphragm[199]. (f) The sensing probe based on a quartz tuning fork enhanced photoacoustic spectroscopy [201].

8. Other Sensors

The EFPI is essentially a universal sensing configuration and has been employed for the measurement of a diverse array of physical, chemical, and biological parameters. In this review, we focus on the air-gap EFPI sensing technologies involving the assistance of a mechanical transducer. A broader overview of the application scope of EFPI sensors can be found in [12]. Here, we have shown a few other interesting applications of EFPI as follows.

A simple and high-performance magnetic field sensor was reported by simply placing two well-cleaved SMFs and bonding them to the surface of a Terfenol-D slab [202]. The stretch of the Terfenol-D slab directly changes the cavity length of the formed EFPI, leading to an ultra-high sensitivity of 854.73 pm/Oe (wavelength shift/magnetic field change). Taking advantage of the magneto-volume effect of magnetic fluid, a fast and vector magnetic field sensor was successfully developed by directly using the magnitude fluid as the second reflector together with a cleaved SMF to form the EFPI [203, 204]. The concave surface of the magnetic fluid varies under different directions of magnetic field, as illustrated in Fig. 13.

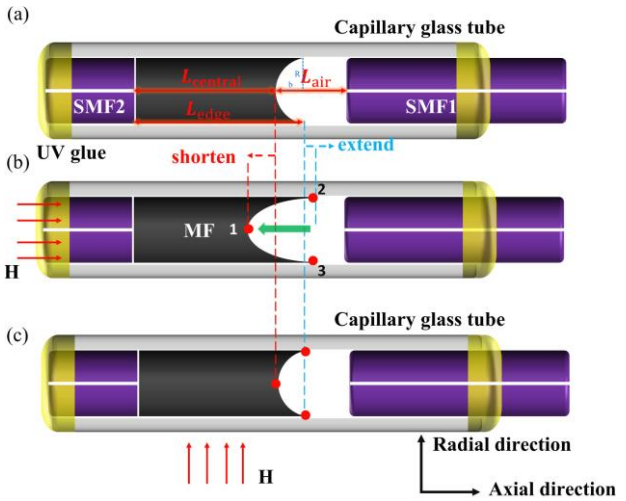

Fig. 13. EFPI vector magnetic field sensor [203]. Schematic diagrams of the sensor under (a) zero field, (b) the axial field, and (c) the radial field.

The uses of EFPI for sensing air flow and liquid flow were also explored. The structure of the EFPI-based air flow sensor was quite simple, where two well-cleaved SMFs are aligned against each other, forming a micro cavity [205], as shown in Fig. 14(a). A micro airflow causes an extremely small pressure difference in the air gap, making the two fiber endfaces tilt upwards and therefore changing the effective cavity length. The prototype sensor demonstrated a high sensitivity of 33.17 $nm/(m\ s^{-1})$ in a range of 0-1.2 m/s. In the case of the liquid flow

sensor, a hollow capillary tube is spliced to a lead-in SMF and cleaved with a certain length attached to the SMF [206]. The free end of the capillary is fine-tuned using the arc discharge technique to obtain a small access hole, as shown in Fig. 14(b). When the sensor head is dipped into the liquid and pulled out, a small volume of liquid (less than 50 pL) flows into the cavity and then leaks out, and the air-liquid interface serves as the second reflector of the formed EFPI. The leaking dynamics are precisely monitored by the EFPI principle, from which the viscosity information of the liquid could be inferred. The simple and high-sensitivity optical fiber viscometer represents an alternative to other modern devices.

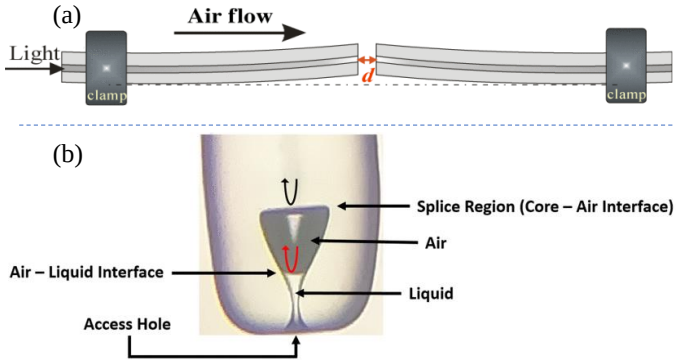

Fig. 14. EFPI flow sensors. (a) Air flow sensor [205]. (b) Liquid viscosity sensor [206].

A similar structure to the diaphragm-EFPI pressure sensor was also employed for humidity sensing, as given in Fig. 15 [207]. A hollow cavity is first fabricated on the tip of an optical fiber with the assistance of a hollow core fiber. A thin layer of moisture-sensitive natural polymer chitosan is then deposited on the top surface of the cavity to form a low-fineness Fabry-Perot sensor. The working principle of the humidity sensor relies on the swelling effect of the chitosan film when it is subject to different levels of humidity. The prototype device with a film thickness of 6.2 μm and a cavity length of 25 μm revealed a sensitivity of 0.13 nm/%RH (wavelength shift/humidity change) in a range of 20%RH-95%RH with a fast response time of 380 ms. Other humidity-sensitive materials such as graphene oxide [208] and polyimide [209] were explored to improve the sensor performance. For example, using a 300-nm-thick graphene oxide film, an ultrafast response of 60 ms was achieved [208], while a high sensitivity of 1.3 nm/%RH was realized using a polyimide film [209].

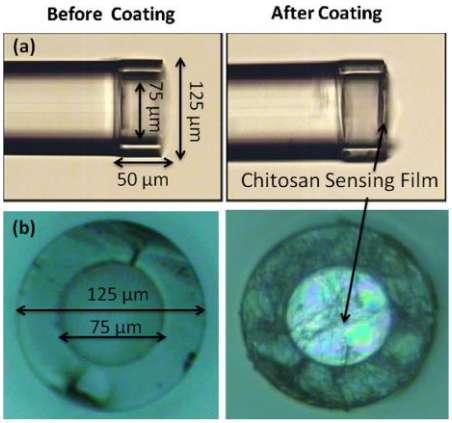

Fig. 15. EFPI humidity sensor [207]. (a) Side view of the proposed sensor before and after coating with chitosan. (b) Cross-section view of the proposed sensor before and after coating with chitosan.

IV. Future Perspectives

It is worth mentioning that many solutions to measuring these physical quantities have also been proposed and demonstrated based on FBG technologies [62, 63]. In those sensor designs, FBGs are integrated with various mechanical transducers. The strain field changes in response to external perturbations, which are then measured by the bonded FBG. However, the measurement sensitivity and resolution are limited because a strain transfer mechanism is always involved in the sensor operation. In the case of EFPI sensors, the deflection or displacement of the transducer subject to external perturbations is directly monitored based on the interference principle in a non-contact mode, thus featuring high sensitivity.

Another key element that affects the sensor performance (e.g., resolution and update rate) is the signal demodulation algorithm, especially when real-time measurements are desired. Different demodulation techniques, such as intensity demodulation, phase demodulation, absolute cavity length demodulation, etc., have been studied in depth, and a comprehensive review of the recent development of these techniques can be found in [23], where multiplexing techniques of EFPI sensors are also discussed. Common strategies employed to achieve FPI-based multi-point measurements include frequency division multiplexing, wavelength division multiplexing, and space division multiplexing. On the other hand, recent years have witnessed remarkable improvements in the study of microwave photonics, and the potential of microwave photonics for the demodulation of FPI sensors has also been explored [210-216]. Both static and dynamic interrogation of FPI sensors (e.g., up to tens of kHz) has been realized based on microwave photonics. Thus, combining the EFPI sensing modality with the microwave photonics-based demodulation approach, new generations of multiplexed EFPI sensors with high sensitivity, fast response, large capacity, and relatively low cost are expected to emerge.

One of the limiting aspects of EFPI sensors is their applications in extremely high-temperature environments. This is because the majority of EFPI sensors are based on SMFs with a softening point at 800 °C. In recent years, researchers have been trying to develop sapphire fiber-based EFPI sensors for the measurement of temperature and pressure above 1000 °C [217]. However, due to the highly multimode nature and high cost of sapphire fibers, the sensing performance of sapphire fiber-based EFPI sensors is not yet on par with SMF-based EFPI devices. To address the limitation of high-temperature applications of SMF-based EFPI sensors, a hollow coaxial cable-based Fabry-Perot interferometer working at the microwave frequency was recently proposed [218]. Two reflectors were fabricated in a microwave transmission line, i.e., the all-stainless-steel coaxial cable, to form a Fabry-Perot cavity. By using a movable reflector, displacement measurements up to 1000 °C were successfully demonstrated by tracking the resonance frequency of the microwave EFPI. However, Due to the long operating wavelength (~meter scale), the displacement measurement resolution of the prototype device was limited to 1 μm, which is at least three orders of

magnitude lower than the optical fiber EFPI device. Very recently, a new scheme was proposed to enhance the displacement resolution of microwave EFPI based on fringing electric field-matter interaction [219, 220]. A detailed comparison between the improved microwave EFPI and optical fiber EFPI can be found in [219]. We envision that by combining the EFPI sensing technologies and the microwave EFPI principle, a new generation of low-cost and high-sensitivity sensors can be developed that are suitable for ultra-high temperature applications (>1000 °C).

V. Conclusion

In summary, we have reviewed the recent progress of the development of highly sensitive air-gap EFPI sensors with the assistance of judicious mechanical transducers. Sensors targeting different physical quantities, including displacement, strain, force, tilt, acceleration (vibration), pressure, and acoustic, are discussed in detail. It is shown that the EFPI principle is indeed a universal strategy for developing high-sensitivity and low-cost fiber-optic sensors. The key element that determines the performance of an EFPI sensor is the transducer (e.g., a diaphragm for a pressure sensor). Thus, great efforts have been made in optimizing the structural design and material selection of the transducer, as reviewed in this article. A few other sensors developed based on the EFPI principle for the measurement of the magnetic field, flow, and humidity are discussed in brief. Perspectives on further advancement of EFPI sensing technologies are also discussed.

References

[1] C. Fabry and A. Pérot, "Sur les franges des lames minces argentées et leur application à la mesure de petites épaisseurs d'air," *Ann. Chim. Phys*, vol. 12, no. 459-501, 1897.

[2] H. Pfeifer *et al.*, "Achievements and perspectives of optical fiber Fabry–Perot cavities," *Applied Physics B*, vol. 128, no. 2, pp. 1-15, 2022.

[3] S. W. Corzine, R. S. Geels, J. W. Scott, R.-H. Yan, and L. A. Coldren, "Design of Fabry-Perot surface-emitting lasers with a periodic gain structure," *IEEE Journal of Quantum Electronics*, vol. 25, no. 6, pp. 1513-1524, 1989.

[4] H. D. Kim, S.-G. Kang, and C.-H. Le, "A low-cost WDM source with an ASE injected Fabry-Perot semiconductor laser," *IEEE Photonics Technology Letters*, vol. 12, no. 8, pp. 1067-1069, 2000.

[5] J. Javaloyes and S. Balle, "Mode-locking in semiconductor Fabry-Perot lasers," *IEEE Journal of Quantum Electronics*, vol. 46, no. 7, pp. 1023-1030, 2010.

[6] P. Atherton, N. K. Reay, J. Ring, and T. Hicks, "Tunable fabry-perot filters," *Optical Engineering*, vol. 20, no. 6, p. 206806, 1981.

[7] S. Irmer *et al.*, "Ultralow biased widely continuously tunable fabry-Perot filter," *IEEE Photonics Technology Letters*, vol. 15, no. 3, pp. 434-436, 2003.

[8] J. S. Milne, J. M. Dell, A. J. Keating, and L. Faraone, "Widely tunable MEMS-based Fabry–Perot filter," *Journal of microelectromechanical systems*, vol. 18, no. 4, pp. 905-913, 2009.

[9] Y.-J. Rao, "Recent progress in fiber-optic extrinsic Fabry–Perot interferometric sensors," *Optical Fiber Technology*, vol. 12, no. 3, pp. 227-237, 2006.

[10] T. Yoshino, K. Kurosawa, K. Itoh, and T. Ose, "Fiber-optic Fabry-Perot interferometer and its sensor applications," *IEEE Transactions on Microwave Theory and Techniques*, vol. 30, no. 10, pp. 1612-1621, 1982.

[11] G. Hernández, *Fabry-perot interferometers* (no. 3). Cambridge University Press, 1988.

[12] M. Islam, M. M. Ali, M.-H. Lai, K.-S. Lim, and H. Ahmad, "Chronology of Fabry-Perot interferometer fiber-optic sensors and their applications: a review," *Sensors*, vol. 14, no. 4, pp. 7451-7488, 2014.

[13] W. Chen, X. Lei, W. Zhang, X. Liu, and C. Liao, "Recent Progress of Optical Fiber Fabry-Perot Sensors," *Acta Optica Sinica*, vol. 38, no. 3, p. 0328010, 2018.

[14] Y.-J. Rao, Z.-L. Ran, and Y. Gong, *Fiber-Optic Fabry–Perot Sensors: An Introduction*. CRC Press, 2017.

[15] Y.-J. Rao, Z.-L. Ran, and Y. Gong, *Fiber-optic fabry-perot sensors: An introduction*. CRC Press, 2017.

[16] J. Ma, M. Zhao, X. Huang, H. Bae, Y. Chen, and M. Yu, "Low cost, high performance white-light fiber-optic hydrophone system with a trackable working point," *Optics express*, vol. 24, no. 17, pp. 19008-19019, 2016.

[17] A. Wang, H. Xiao, J. Wang, Z. Wang, W. Zhao, and R. May, "Self-calibrated interferometric-intensity-based optical fiber sensors," *Journal of lightwave technology*, vol. 19, no. 10, p. 1495, 2001.

[18] X. Mao, S. Yuan, P. Zheng, and X. Wang, "Stabilized fiber-optic Fabry–Perot acoustic sensor based on improved wavelength tuning technique," *Journal of Lightwave Technology*, vol. 35, no. 11, pp. 2311-2314, 2017.

[19] Z. Yu and A. Wang, "Fast white light interferometry demodulation algorithm for low-finesse Fabry–Pérot sensors," *IEEE Photonics Technology Letters*, vol. 27, no. 8, pp. 817-820, 2015.

[20] J. Xie, F. Wang, Y. Pan, J. Wang, Z. Hu, and Y. Hu, "High resolution signal-processing method for extrinsic Fabry–Perot interferometric sensors," *Optical Fiber Technology*, vol. 22, pp. 1-6, 2015.

[21] C. Li, S. Chen, and Y. Zhu, "Maximum likelihood estimation of optical path length in spectral interferometry," *Journal of Lightwave Technology*, vol. 35, no. 22, pp. 4880-4887, 2017.

[22] Y. Wu, L. Xia, N. Cai, and L. Zhu, "A highly precise demodulation method for fiber Fabry-Perot cavity through spectrum reconstruction," *IEEE Photonics Technology Letters*, vol. 30, no. 5, pp. 435-438, 2017.

[23] Q. Liu and W. Peng, "Fast interrogation of dynamic low-finesse Fabry-Perot interferometers: A review," *Microwave and Optical Technology Letters*, vol. 63, no. 9, pp. 2279-2291, 2021.

[24] C. Leitão *et al.*, "Cortisol in-fiber ultrasensitive plasmonic immunosensing," *IEEE Sensors Journal*, vol. 21, no. 3, pp. 3028-3034, 2020.

[25] V. Kumar, S. K. Raghuwanshi, and S. Kumar, "Recent Advances in Carbon Nanomaterials Based SPR Sensor for Biomolecules and Gas Detection-A Review," *IEEE Sensors Journal*, 2022.

[26] Z. Wang *et al.*, "Novel Optical Fiber-Based Structures for Plasmonics Sensors," *Biosensors*, vol. 12, no. 11, p. 1016, 2022.

[27] M. Li, R. Singh, Y. Wang, C. Marques, B. Zhang, and S. Kumar, "Advances in Novel Nanomaterial-Based Optical Fiber Biosensors—A Review," *Biosensors*, vol. 12, no. 10, p. 843, 2022.

[28] A. K. Vyas, R. K. Gangwar, and S. Kumar, "Elliptical air hole PCF-based low-cost sensor for refractive index and temperature detection: Design and analysis," *Optical Fiber Technology*, vol. 73, p. 103060, 2022.

[29] A. Shadab, S. K. Raghuwanshi, and S. Kumar, "Advances in Micro-Fabricated Fiber Bragg Grating for Detection of Physical, Chemical and Biological Parameters–A Review," *IEEE Sensors Journal*, 2022.

[30] V. Kumar, S. K. Raghuwanshi, and S. Kumar, "Advances in nanocomposite thin-film-based optical fiber sensors for environmental health monitoring-a review," *IEEE Sensors Journal*, 2022.

[31] M. D. Nadeem, S. K. Raghuwanshi, and S. Kumar, "Recent advancement of phase shifted fiber Bragg grating sensor for ultrasonic wave application: A review," *IEEE Sensors Journal*, 2022.

[32] M. Li, R. Singh, M. S. Soares, C. Marques, B. Zhang, and S. Kumar, "Convex fiber-tapered seven core fiber-convex fiber (CTC) structure-based biosensor for creatinine detection in aquaculture," *Optics Express*, vol. 30, no. 8, pp. 13898-13914, 2022.

[33] N. Agrawal, C. Saha, C. Kumar, R. Singh, B. Zhang, and S. Kumar, "Development of uric acid sensor using copper oxide and silver nanoparticles immobilized SMSMS fiber structure-based probe," *IEEE Transactions on Instrumentation and Measurement*, vol. 69, no. 11, pp. 9097-9104, 2020.

[34] L. Singh, R. Singh, B. Zhang, B. K. Kaushik, and S. Kumar, "Localized surface plasmon resonance based hetero-core optical fiber sensor structure for the detection of L-cysteine," *IEEE Transactions on Nanotechnology*, vol. 19, pp. 201-208, 2020.

[35] B. K. Kaushik *et al.*, "Detection of collagen-IV using highly reflective metal nanoparticles—Immobilized photosensitive optical fiber-based MZI structure," *IEEE Transactions on NanoBioscience*, vol. 19, no. 3, pp. 477-484, 2020.

[36] S. Kumar, R. Singh, B. K. Kaushik, N.-k. Chen, Q. S. Yang, and X. Zhang, "LSPR-based cholesterol biosensor using hollow core fiber structure," *IEEE Sensors Journal*, vol. 19, no. 17, pp. 7399-7406, 2019.

[37] C. Zhu, R. E. Gerald, and J. Huang, "Metal-organic framework materials coupled to optical fibers for chemical sensing: A review," *IEEE sensors journal*, vol. 21, no. 18, pp. 19647-19661, 2021.

[38] A. Urrutia, I. Del Villar, P. Zubiate, and C. R. Zamarreño, "A comprehensive review of optical fiber refractometers: Toward a standard comparative criterion," *Laser & Photonics Reviews*, vol. 13, no. 11, p. 1900094, 2019.

[39] F. Chiavaioli and D. Janner, "Fiber optic sensing with lossy mode resonances: Applications and perspectives," *Journal of Lightwave Technology*, vol. 39, no. 12, pp. 3855-3870, 2021.

[40] F. Esposito, "Chemical sensors based on long period fiber gratings: A review," *Results in Optics*, vol. 5, p. 100196, 2021.

[41] F. Esposito, A. Srivastava, L. Sansone, M. Giordano, S. Campopiano, and A. Iadicicco, "Label-free biosensors based on long period fiber gratings: a review," *IEEE Sensors Journal*, vol. 21, no. 11, pp. 12692-12705, 2020.

[42] T. Wei, Y. Han, Y. Li, H.-L. Tsai, and H. Xiao, "Temperature-insensitive miniaturized fiber inline Fabry-Perot interferometer for highly sensitive refractive index measurement," *Optics Express*, vol. 16, no. 8, pp. 5764-5769, 2008.

[43] H.-T. Kim, W. Hwang, Y. Liu, and M. Yu, "Ultracompact gas sensor with metal-organic-framework-based differential fiber-optic Fabry-Perot nanocavities," *Optics Express*, vol. 28, no. 20, pp. 29937-29947, 2020.

[44] C. Zhu, J. A. Perman, R. E. Gerald, S. Ma, and J. Huang, "Chemical detection using a metal–organic framework single crystal coupled to an optical fiber," *ACS applied materials & interfaces*, vol. 11, no. 4, pp. 4393-4398, 2019.

[45] H. Z. Yang, X. G. Qiao, D. Luo, K. S. Lim, W. Chong, and S. W. Harun, "A review of recent developed and applications of plastic fiber optic displacement sensors," *Measurement*, vol. 48, pp. 333-345, 2014.

[46] X. Zhou and Q. Yu, "Wide-range displacement sensor based on fiber-optic Fabry–Perot interferometer for subnanometer measurement," *IEEE sensors journal*, vol. 11, no. 7, pp. 1602-1606, 2010.

[47] C. J. Moreno-Hernández, D. Monzón-Hernández, A. Martínez-Ríos, D. Moreno-Hernández, and J. Villatoro, "Long-range interferometric displacement sensing with tapered optical fiber tips," *IEEE Photonics Technology Letters*, vol. 27, no. 4, pp. 379-382, 2014.

[48] K. Tian *et al.*, "Miniature Fabry–Perot interferometer based on a movable microsphere reflector," *Optics Letters*, vol. 45, no. 3, pp. 787-790, 2020.

[49] C. Zhu *et al.*, "A displacement sensor with centimeter dynamic range and submicrometer resolution based on an optical interferometer," *IEEE Sensors Journal*, vol. 17, no. 17, pp. 5523-5528, 2017.

[50] C. Zhu *et al.*, "An optical interferometric triaxial displacement sensor for structural health monitoring: Characterization of sliding and debonding for a delamination process," *Sensors*, vol. 17, no. 11, p. 2696, 2017.

[51] M. C. Alonso-Murias *et al.*, "Long-range multicore optical fiber displacement sensor," *Optics Letters*, vol. 46, no. 9, pp. 2224-2227, 2021.

[52] Y. Yang, X. Zhang, L. Yang, Y. Yu, Z. Wang, and T. Wang, "Ultrahigh-sensitivity displacement sensing enabled by the Vernier effect with inhibited antiresonance," *Optics Letters*, vol. 46, no. 5, pp. 1053-1056, 2021.

[53] C. Zhu and J. Huang, "An optical fiber extrinsic Fabry-Perot interferometer based displacement sensor with centimeter measurement range," in *Sensors and Smart Structures Technologies for Civil, Mechanical, and Aerospace Systems 2018*, 2018, vol. 10598: International Society for Optics and Photonics, p. 105983J.

[54] C. Zhu and J. Huang, "A three-dimensional sliding and debonding sensor based on triaxial optical fiber Fabry-Perot interferometers," in *Sensors and Smart Structures Technologies for Civil, Mechanical, and Aerospace Systems 2018*, 2018, vol. 10598: International Society for Optics and Photonics, p. 105983A.

[55] F. Tang, Z. Li, Y. Tang, Y. Chen, and H.-N. Li, "Simultaneous measurement of shrinkage and coefficient of thermal expansion of mortar based on EFPI sensors with nanometer resolution," *Measurement*, vol. 152, p. 107376, 2020.

[56] C. Guo, Y. Zhang, M. Klegseth, J. Gao, and G. Chen, "Micrometer-accuracy 2D displacement interferometer with plasmonic metasurface resonators," *Opt. Lett.*, vol. 45, no. 23, pp. 6474-6477, 2020.

[57] Z. Xu, Z. Wang, L. Chen, J. Fan, L. Tu, and Z. Zhou, "Two-dimensional displacement sensor based on a dual-cavity Fabry-Perot interferometer," *Journal of Lightwave Technology*, 2021.

[58] Z. Wang *et al.*, "Highly precise in-plane displacement sensor based on an asymmetric fiber Fabry–Perot interferometer," *Opt. Lett.*, vol. 46, no. 16, pp. 3945-3948, 2021.

[59] C. Zhu, H. Deng, Z. Ding, J. Huang, and Z. Zhang, "Optical fiber Fabry–Perot interferometer coupled to a 3-D integrated waveguide for 3-D position sensing," *Opt. Lett.*, vol. 46, no. 23, pp. 5838-5841, 2021.

[60] M. F. Bado and J. R. Casas, "A review of recent distributed optical fiber sensors applications for civil engineering structural health monitoring," *Sensors*, vol. 21, no. 5, p. 1818, 2021.

[61] H. Guo, G. Xiao, N. Mrad, and J. Yao, "Fiber optic sensors for structural health monitoring of air platforms," *Sensors*, vol. 11, no. 4, pp. 3687-3705, 2011.

[62] J. K. Sahota, N. Gupta, and D. Dhawan, "Fiber Bragg grating sensors for monitoring of physical parameters: A comprehensive review," *Optical Engineering*, vol. 59, no. 6, p. 060901, 2020.

[63] S. J. Mihailov, "Fiber Bragg grating sensors for harsh environments," *Sensors*, vol. 12, no. 2, pp. 1898-1918, 2012.

[64] P. Lu *et al.*, "Distributed optical fiber sensing: Review and perspective," *Applied Physics Reviews*, vol. 6, no. 4, p. 041302, 2019.

[65] Z. Ding *et al.*, "Distributed optical fiber sensors based on optical frequency domain reflectometry: A review," *Sensors*, vol. 18, no. 4, p. 1072, 2018.

[66] T. Paixão, F. Araújo, and P. Antunes, "Highly sensitive fiber optic temperature and strain sensor based on an intrinsic Fabry–Perot interferometer fabricated by a femtosecond laser," *Optics Letters*, vol. 44, no. 19, pp. 4833-4836, 2019.

[67] M. F. Domingues *et al.*, "Cost-effective optical fiber pressure sensor based on intrinsic Fabry-Perot interferometric micro-cavities," *Optical Fiber Technology*, vol. 42, pp. 56-62, 2018.

[68] Y. Huang, T. Wei, Z. Zhou, Y. Zhang, G. Chen, and H. Xiao, "An extrinsic Fabry–Perot interferometer-based large strain sensor with high resolution," *Measurement science and technology*, vol. 21, no. 10, p. 105308, 2010.

[69] S. Liu *et al.*, "High-sensitivity strain sensor based on in-fiber rectangular air bubble," *Scientific reports*, vol. 5, no. 1, pp. 1-7, 2015.

[70] F. Favero, L. Araujo, G. Bouwmans, V. Finazzi, J. Villatoro, and V. Pruneri, "Spheroidal Fabry-Perot microcavities in optical fibers for high-sensitivity sensing," *Optics Express*, vol. 20, no. 7, pp. 7112-7118, 2012.

[71] S. Pevec and D. Donlagic, "All-fiber, long-active-length Fabry-Perot strain sensor," *Optics Express*, vol. 19, no. 16, pp. 15641-15651, 2011.

[72] M. S. Ferreira, J. Bierlich, J. Kobelke, K. Schuster, J. L. Santos, and O. Frazão, "Towards the control of highly sensitive Fabry-Pérot strain sensor based on hollow-core ring photonic crystal fiber," *Optics express*, vol. 20, no. 20, pp. 21946-21952, 2012.

[73] K. Zhou *et al.*, "High-sensitivity strain sensor with an in-fiber air-bubble Fabry-Perot interferometer," *Applied Physics Letters*, vol. 113, no. 18, p. 181901, 2018.

[74] C. Lang, Y. Liu, K. Cao, and S. Qu, "Temperature-insensitive optical fiber strain sensor with ultra-low detection limit based on capillary-taper temperature compensation structure," *Optics Express*, vol. 26, no. 1, pp. 477-487, 2018.

[75] Y. Du, Y. Chen, Y. Zhuang, C. Zhu, F. Tang, and J. Huang, "Probing nanostrain via a mechanically designed optical fiber interferometer," *IEEE Photonics Technology Letters*, vol. 29, no. 16, pp. 1348-1351, 2017.

[76] C. Zhu, Y. Chen, Y. Zhuang, F. Tang, and J. Huang, "An embeddable strain sensor with 30 nano-strain resolution based on optical interferometry," *Inventions*, vol. 3, no. 2, p. 20, 2018.

[77] Y. Du, Y. Chen, C. Zhu, Y. Zhuang, and J. Huang, "An embeddable optical strain gauge based on a buckled beam," *Review of Scientific Instruments*, vol. 88, no. 11, p. 115002, 2017.

[78] S. Aiguo and F. Liyue, "Multi-dimensional force sensor for haptic interaction: A review," *Virtual Reality & Intelligent Hardware*, vol. 1, no. 2, pp. 121-135, 2019.

[79] A. A. Abushagur, N. Arsad, M. I. Reaz, and A. Bakar, "Advances in bio-tactile sensors for minimally invasive surgery using the fibre Bragg grating force sensor technique: A survey," *Sensors*, vol. 14, no. 4, pp. 6633-6665, 2014.

[80] X. Liu, I. I. Iordachita, X. He, R. H. Taylor, and J. U. Kang, "Miniature fiber-optic force sensor based on low-coherence Fabry-Pérot interferometry for vitreoretinal microsurgery," *Biomedical optics express*, vol. 3, no. 5, pp. 1062-1076, 2012.

[81] U.-X. Tan, B. Yang, R. Gullapalli, and J. P. Desai, "Triaxial MRI-compatible fiber-optic force sensor," *IEEE Transactions on Robotics*, vol. 27, no. 1, pp. 65-74, 2010.

[82] P. Polygerinos, L. D. Seneviratne, R. Razavi, T. Schaeffter, and K. Althoefer, "Triaxial catheter-tip force sensor for MRI-guided cardiac procedures," *IEEE/ASME Transactions on mechatronics*, vol. 18, no. 1, pp. 386-396, 2012.

[83] H. Su *et al.*, "Fiber-optic force sensors for MRI-guided interventions and rehabilitation: A review," *IEEE sensors journal*, vol. 17, no. 7, pp. 1952-1963, 2017.

[84] N. O. Ulgen, D. Uzun, and O. Kocaturk, "Phantom study of a fiber optic force sensor design for biopsy needles under MRI," *Biomedical Optics Express*, vol. 10, no. 1, pp. 242-251, 2019.

[85] S. Gao *et al.*, "Microfiber-enabled in-line Fabry–Pérot interferometer for high-sensitive force and refractive index sensing," *Journal of lightwave technology*, vol. 32, no. 9, pp. 1682-1688, 2014.

[86] M. Llera *et al.*, "Liquid-air based Fabry-Pérot cavity on fiber tip sensor," *Optics express*, vol. 24, no. 8, pp. 8054-8065, 2016.

[87] Y. Liu, C. Lang, X. Wei, and S. Qu, "Strain force sensor with ultra-high sensitivity based on fiber inline Fabry-Perot micro-cavity plugged by cantilever taper," *Optics Express*, vol. 25, no. 7, pp. 7797-7806, 2017.

[88] J. N. Dash, Z. Liu, D. S. Gunawardena, and H.-Y. Tam, "Fabry–Perot cavity-based contact force sensor with high precision and a broad operational range," *Optics letters*, vol. 44, no. 14, pp. 3546-3549, 2019.

[89] A. J. Thompson, M. Power, and G.-Z. Yang, "Micro-scale fiber-optic force sensor fabricated using direct laser writing and calibrated using machine learning," *Optics Express*, vol. 26, no. 11, pp. 14186-14200, 2018.

[90] S. Pevec and D. Donlagic, "Miniature all-fiber force sensor," *Optics Letters*, vol. 45, no. 18, pp. 5093-5096, 2020.

[91] M. Zou *et al.*, "Fiber-tip polymer clamped-beam probe for high-sensitivity nanoforce measurements," *Light: Science & Applications*, vol. 10, no. 1, pp. 1-12, 2021.

[92] O. R. Ranjbar-Naeini, H. Latifi, M. I. Zibaii, and A. Mousavian, "Measurement of milli-Newton axial force and temperature using a hybrid microsilica sphere Fabry–Perot sensor," *Optics letters*, vol. 43, no. 21, pp. 5210-5213, 2018.

[93] D. Iannuzzi, S. Deladi, V. Gadgil, R. G. Sanders, H. Schreuders, and M. C. Elwenspoek, "Monolithic fiber-top sensor for critical environments and standard applications," *Applied physics letters*, vol. 88, no. 5, p. 053501, 2006.

[94] K. B. Gavan *et al.*, "Top-down approach to fiber-top cantilevers," *Optics letters*, vol. 36, no. 15, pp. 2898-2900, 2011.

[95] D. Chavan *et al.*, "Ferrule-top atomic force microscope," *Review of Scientific Instruments*, vol. 81, no. 12, p. 123702, 2010.

[96] Y. Tang, J. Guo, Y. Chen, and J. Huang, "Optical Interferometric Force Sensor Based on a Buckled Beam," *IEEE Sensors Journal*, vol. 22, no. 2, pp. 1301-1308, 2021.

[97] S. Łuczak and M. Ekwińska, "Electric-contact tilt sensors: A review," *Sensors*, vol. 21, no. 4, p. 1097, 2021.

[98] C.-L. Lee, Y.-C. Zheng, C.-L. Ma, H.-J. Chang, and C.-F. Lee, "Dynamic micro-air-bubble drifted in a liquid core fiber Fabry-Pérot interferometer for directional fiber-optic level meter," *Applied Physics Letters*, vol. 102, no. 19, p. 193504, 2013.

[99] K. Cao, Y. Liu, and S. Qu, "Ultrasensitive fiber tilt sensor based on a mobile inscribed microbubble along the arc-shaped inwall of the microcavity," *Optics Letters*, vol. 42, no. 21, pp. 4418-4421, 2017.

[100] X. Ji, Y. Liu, K. Cao, Y. Liao, Y. Li, and S. Qu, "Laser-induced suspension of a microbubble in a liquid-filled fiber microcavity for large-range tilt sensing," *Optics Letters*, vol. 45, no. 8, pp. 2303-2306, 2020.

[101] C. Li, X. Li, X. Yu, X. Peng, T. Lan, and S. Fan, "Room-temperature wide measurement-range optical fiber fabry–perot tilt sensor with liquid marble," *IEEE Sensors Journal*, vol. 18, no. 1, pp. 170-177, 2017.

[102] J. Pan, Q. Nan, S. Li, and Z. Hao, "Development of a high resolution optical-fiber tilt sensor by FP filter," in *2017 25th Optical Fiber Sensors Conference (OFS)*, 2017: IEEE, pp. 1-4.

[103] P. Cui, W. Zhang, Y. Song, and Y. Ma, "Optical Fiber Fabry-Perot Inclinometer Based on White Light Interferometry," in *Asia Communications and Photonics Conference*, 2018: Optical Society of America, p. Su2A. 85.

[104] Y. Yang, E. Wang, K. Chen, Z. Yu, and Q. Yu, "Fiber-optic Fabry–Perot sensor for simultaneous measurement of tilt angle and vibration acceleration," *IEEE Sensors Journal*, vol. 19, no. 6, pp. 2162-2169, 2018.

[105] S. Wang, Y. Yang, L. Mohanty, R.-B. Jin, and P. Lu, "Ultrasensitive fiber optic inclinometer based on dynamic Vernier effect using push-pull configuration," *IEEE Transactions on Instrumentation and Measurement*, 2022.

[106] Y. Zhuang, Y. Chen, C. Zhu, R. E. Gerald, and J. Huang, "Probing changes in tilt angle with 20 nanoradian resolution using an extrinsic Fabry-Perot interferometer-based optical fiber inclinometer," *Optics express*, vol. 26, no. 3, pp. 2546-2556, 2018.

[107] C. Zhu, R. E. Gerald II, Y. Chen, and J. Huang, "One-dimensional sensor learns to sense three-dimensional space," *Optics Express*, vol. 28, no. 13, pp. 19374-19389, 2020.

[108] C. Zhu and J. Huang, "Smart Fiber-optic Inclinometer," in *Conference on Lasers and Electro-Optics*, Washington, DC, 2020/05/10 2020: Optica Publishing Group, in OSA Technical Digest, p. AM1K.2, doi: 10.1364/CLEO_AT.2020.AM1K.2. [Online]. Available: http://opg.optica.org/abstract.cfm?URI=CLEO_AT-2020-AM1K.2

[109] C. Zhu, R. E. Gerald, and J. Huang, "Ultra-high Sensitivity 1D Sensor for Sensing 3D Space," in *Optical Fiber Sensors Conference 2020 Special Edition*, Washington, DC, G. W. A. D. M. Cranch and P. Dragic, Eds., 2020/06/08 2020: Optica Publishing Group, in OSA Technical Digest, p. Th4.43, doi: 10.1364/OFS.2020.Th4.43. [Online]. Available: http://opg.optica.org/abstract.cfm?URI=OFS-2020-Th4.43

[110] Y. Zhuang, Y. Chen, C. Zhu, R. E. Gerald, Y. Tang, and J. Huang, "A high-resolution 2-D fiber optic inclinometer for structural health monitoring applications," *IEEE Transactions on Instrumentation and Measurement*, vol. 69, no. 9, pp. 6544-6555, 2020.

[111] Y. Yang, X. Ma, K. Chen, E. Wang, Z. Yu, and Q. Yu, "A high-resolution dynamic fiber-optic inclinometer," *Sensors and Actuators A: Physical*, vol. 283, pp. 305-312, 2018.

[112] K. Hirata, H. Niitsuma, and M. Esashi, "Silicon micromachined fiber-optic accelerometer for downhole seismic measurement," *IEEJ Transactions on Sensors and Micromachines*, vol. 120, no. 12, pp. 576-581, 2000.

[113] T. K. Gangopadhyay, "Prospects for fibre Bragg gratings and Fabry-Perot interferometers in fibre-optic vibration sensing," *Sensors and Actuators A: Physical*, vol. 113, no. 1, pp. 20-38, 2004.

[114] P. Jia and D. Wang, "Self-calibrated non-contact fibre-optic Fabry–Perot interferometric vibration displacement sensor system using laser emission frequency modulated phase generated carrier demodulation scheme," *Measurement Science and Technology*, vol. 23, no. 11, p. 115201, 2012.

[115] Q. Lin, L. Chen, S. Li, and X. Wu, "A high-resolution fiber optic accelerometer based on intracavity phase-generated carrier (PGC) modulation," *Measurement Science and Technology*, vol. 22, no. 1, p. 015303, 2010.

[116] Z. Zhao, Z. Yu, K. Chen, and Q. Yu, "A fiber-optic fabry-perot accelerometer based on high-speed white light interferometry

demodulation," *Journal of Lightwave Technology*, vol. 36, no. 9, pp. 1562-1567, 2018.

[117] F. Wang *et al.*, "All-optical accelerometer based on micromachined silicon wafer," in *Fiber Optic Sensing and Optical Communication*, 2018, vol. 10849: International Society for Optics and Photonics, p. 108491I.

[118] M. D. Pocha, G. A. Meyer, C. F. McConaghy, S. P. Swierkowski, and J. D. Wolfe, "Miniature accelerometer and multichannel signal processor for fiberoptic Fabry–Pérot sensing," *IEEE Sensors Journal*, vol. 7, no. 2, pp. 285-292, 2007.

[119] X. Zeng, Y. Wu, C.-l. Hou, and G.-g. Yang, "High-finesse displacement sensor and a theoretical accelerometer model based on a fiber Fabry-Perot interferometer," *Journal of Zhejiang University-SCIENCE A*, vol. 10, no. 4, pp. 589-594, 2009.

[120] P. Zhang, S. Wang, J. Jiang, Z. Li, H. Yang, and T. Liu, "A Fiber-Optic Accelerometer Based on Extrinsic Fabry-Perot Interference for Low Frequency Micro-Vibration Measurement," *IEEE Photonics Journal*, vol. 14, no. 4, pp. 1-6, 2022.

[121] Z. Wang, W. Zhang, J. Han, W. Huang, and F. Li, "Diaphragm-based fiber optic Fabry–Perot accelerometer with high consistency," *Journal of Lightwave Technology*, vol. 32, no. 24, pp. 4810-4815, 2014.

[122] S. Li, X. Wu, J. Shi, Q. Ge, G. Zhang, and B. Yu, "Fabry-Perot interferometer based on an aluminum-polyimide composite diaphragm integrated with mass for acceleration sensing," *Ieee Access*, vol. 7, pp. 186510-186516, 2019.

[123] S. Li *et al.*, "Low-cost fiber optic extrinsic Fabry–Perot interferometer based on a polyethylene diaphragm for vibration detection," *Optics Communications*, vol. 457, p. 124332, 2020.

[124] E. Davies, D. S. George, M. C. Gower, and A. S. Holmes, "MEMS Fabry–Pérot optical accelerometer employing mechanical amplification via a V-beam structure," *Sensors and Actuators A: Physical*, vol. 215, pp. 22-29, 2014.

[125] M. Pisco *et al.*, "Opto-mechanical lab-on-fibre seismic sensors detected the Norcia earthquake," *Scientific reports*, vol. 8, no. 1, pp. 1-14, 2018.

[126] F. A. Bruno, M. Pisco, G. Gruca, N. Rijnveld, and A. Cusano, "Opto-mechanical lab-on-fiber accelerometers," *Journal of Lightwave Technology*, vol. 38, no. 7, pp. 1998-2009, 2019.

[127] F. Guzmán Cervantes, L. Kumanchik, J. Pratt, and J. M. Taylor, "High sensitivity optomechanical reference accelerometer over 10 kHz," *Applied Physics Letters*, vol. 104, no. 22, p. 221111, 2014.

[128] O. Gerberding, F. G. Cervantes, J. Melcher, J. R. Pratt, and J. M. Taylor, "Optomechanical reference accelerometer," *Metrologia*, vol. 52, no. 5, p. 654, 2015.

[129] B. Liu *et al.*, "Extrinsic Fabry–Pérot cantilever accelerometer based on micromachined 45° angled fiber," *Journal of Lightwave Technology*, vol. 36, no. 11, pp. 2196-2203, 2018.

[130] Q. Zhang, T. Zhu, Y. Hou, and K. S. Chiang, "All-fiber vibration sensor based on a Fabry–Perot interferometer and a microstructure beam," *JOSA B*, vol. 30, no. 5, pp. 1211-1215, 2013.

[131] G. Gruca, D. Chavan, J. Rector, K. Heeck, and D. Iannuzzi, "Demonstration of an optically actuated ferrule-top device for pressure and humidity sensing," *Sensors and Actuators A: Physical*, vol. 190, pp. 77-83, 2013.

[132] N. Wu, Y. Tian, X. Zou, Y. Zhai, K. Barringhaus, and X. Wang, "A miniature fiber optic blood pressure sensor and its application in in vivo blood pressure measurements of a swine model," *Sensors and Actuators B: Chemical*, vol. 181, pp. 172-178, 2013.

[133] N. Wu *et al.*, "An ultra-fast fiber optic pressure sensor for blast event measurements," *Measurement Science and Technology*, vol. 23, no. 5, p. 055102, 2012.

[134] X. Zou *et al.*, "Ultrafast Fabry–Perot fiber-optic pressure sensors for multimedia blast event measurements," *Applied optics*, vol. 52, no. 6, pp. 1248-1254, 2013.

[135] Q. Yu and X. Zhou, "Pressure sensor based on the fiber-optic extrinsic Fabry-Perot interferometer," *Photonic Sensors*, vol. 1, no. 1, pp. 72-83, 2011.

[136] X. Zhou, Q. Yu, and W. Peng, "Fiber-optic Fabry–Perot pressure sensor for down-hole application," *Optics and Lasers in Engineering*, vol. 121, pp. 289-299, 2019.

[137] S. H. Aref, H. Latifi, M. I. Zibaii, and M. Afshari, "Fiber optic Fabry–Perot pressure sensor with low sensitivity to temperature changes for downhole application," *Optics communications*, vol. 269, no. 2, pp. 322-330, 2007.

[138] Q. Zhao *et al.*, "Adhesive-free bonding fiber optic Fabry–Perot pressure sensor based on oxy-hydrogen flame welding and spiral tube," *Optics Communications*, vol. 476, p. 126307, 2020.

[139] R. Wang and X. Qiao, "Intrinsic Fabry-Pérot interferometer based on concave well on fiber end," *IEEE Photonics Technology Letters*, vol. 26, no. 14, pp. 1430-1433, 2014.

[140] X. Zhang *et al.*, "Membrane-free fiber-optic Fabry-Perot gas pressure sensor with Pa-level resolution," *Optics & Laser Technology*, vol. 150, p. 107940, 2022.

[141] S. Pevec and D. Donlagic, "Miniature fiber-optic Fabry-Perot refractive index sensor for gas sensing with a resolution of 5x10− 9 RIU," *Optics express*, vol. 26, no. 18, pp. 23868-23882, 2018.

[142] Z. Zhang, J. He, B. Du, F. Zhang, K. Guo, and Y. Wang, "Measurement of high pressure and high temperature using a dual-cavity Fabry–Perot interferometer created in cascade hollow-core fibers," *Optics letters*, vol. 43, no. 24, pp. 6009-6012, 2018.

[143] D. Donlagic and E. Cibula, "All-fiber high-sensitivity pressure sensor with SiO 2 diaphragm," *Optics letters*, vol. 30, no. 16, pp. 2071-2073, 2005.

[144] K. Totsu, Y. Haga, and M. Esashi, "Ultra-miniature fiber-optic pressure sensor using white light interferometry," *Journal of Micromechanics and Microengineering*, vol. 15, no. 1, p. 71, 2004.

[145] W. Wang, N. Wu, Y. Tian, C. Niezrecki, and X. Wang, "Miniature all-silica optical fiber pressure sensor with an ultrathin uniform diaphragm," *Optics express*, vol. 18, no. 9, pp. 9006-9014, 2010.

[146] C. Liao *et al.*, "Sub-micron silica diaphragm-based fiber-tip Fabry–Perot interferometer for pressure measurement," *Optics letters*, vol. 39, no. 10, pp. 2827-2830, 2014.

[147] S. Liu *et al.*, "Nano silica diaphragm in-fiber cavity for gas pressure measurement," *Scientific reports*, vol. 7, no. 1, pp. 1-9, 2017.

[148] E. Cibula and D. Đonlagić, "Miniature fiber-optic pressure sensor with a polymer diaphragm," *Applied optics*, vol. 44, no. 14, pp. 2736-2744, 2005.

[149] F. Xu *et al.*, "High-sensitivity Fabry–Perot interferometric pressure sensor based on a nanothick silver diaphragm," (in en), *Optics Letters*, vol. 37, no. 2, p. 133, 2012-01-15 2012, doi: 10.1364/OL.37.000133.

[150] J. Ma, W. Jin, H. L. Ho, and J. Y. Dai, "High-sensitivity fiber-tip pressure sensor with graphene diaphragm," *Optics letters*, vol. 37, no. 13, pp. 2493-2495, 2012.

[151] L. Cheng, C. Wang, Y. Huang, H. Liang, and B.-O. Guan, "Silk fibroin diaphragm-based fiber-tip Fabry-Perot pressure sensor," *Optics express*, vol. 24, no. 17, pp. 19600-19606, 2016.

[152] J. Eom, C.-J. Park, B. H. Lee, J.-H. Lee, I.-B. Kwon, and E. Chung, "Fiber optic Fabry–Perot pressure sensor based on lensed fiber and polymeric diaphragm," *Sensors and Actuators A: Physical*, vol. 225, pp. 25-32, 2015.

[153] C. Luo *et al.*, "An optimized PDMS thin film immersed Fabry-Perot fiber optic pressure sensor for sensitivity enhancement," *Coatings*, vol. 9, no. 5, p. 290, 2019.

[154] X. Wei *et al.*, "Optical fiber gas pressure sensor based on polydimethylsiloxane microcavity," *Journal of Lightwave Technology*, vol. 39, no. 9, pp. 2988-2993, 2021.

[155] X. Cheng, J. N. Dash, D. S. Gunawardena, L. Htein, and H.-Y. Tam, "Silicone rubber based highly sensitive fiber-optic Fabry–Perot interferometric gas pressure sensor," *Sensors*, vol. 20, no. 17, p. 4927, 2020.

[156] Y. Zhang *et al.*, "A High Precision Fiber Optic Fabry–Perot Pressure Sensor Based on AB Epoxy Adhesive Film," in *Photonics*, 2021, vol. 8, no. 12: MDPI, p. 581.

[157] C. Zhu, Y. Chen, Y. Zhuang, G. Fang, X. Liu, and J. Huang, "Optical interferometric pressure sensor based on a buckled beam with low-temperature cross-sensitivity," *IEEE Transactions on Instrumentation and Measurement*, vol. 67, no. 4, pp. 950-955, 2018.

[158] C. Zhu and J. Huang, "Buckled beam based optical interferometric pressure sensor with low temperature cross-sensitivity," in *Sensors and Smart Structures Technologies for Civil, Mechanical, and Aerospace Systems 2018*, 2018, vol. 10598: SPIE, pp. 927-932.

[159] J. Wu, M. Yao, F. Xiong, A. P. Zhang, H.-Y. Tam, and P. K. A. Wai, "Optical fiber-tip Fabry–Perot interferometric pressure sensor based on an in situ μ-printed air cavity," *Journal of Lightwave Technology*, vol. 36, no. 17, pp. 3618-3623, 2018.

[160] Q. Cui, P. Thakur, C. Rablau, I. Avrutsky, and M. M.-C. Cheng, "Miniature optical fiber pressure sensor with exfoliated graphene diaphragm," *IEEE Sensors Journal*, vol. 19, no. 14, pp. 5621-5631, 2019.

[161] C. Zhu, Y. Chen, R. E. Gerald, and J. Huang, "Probing changes in pressure with subpascal resolution using an optical fiber Fabry–Perot interferometer," *IEEE Transactions on Instrumentation and Measurement*, vol. 69, no. 9, pp. 6556-6563, 2020.

[162] J. Xu, G. Pickrell, X. Wang, W. Peng, K. Cooper, and A. Wang, "A novel temperature-insensitive optical fiber pressure sensor for harsh environments," *IEEE Photonics Technology Letters*, vol. 17, no. 4, pp. 870-872, 2005.

[163] B. Yu, D. W. Kim, J. Deng, H. Xiao, and A. Wang, "Fiber Fabry-Perot sensors for detection of partial discharges in power transformers," *Applied optics*, vol. 42, no. 16, pp. 3241-3250, 2003.

[164] M. J. Gander *et al.*, "Embedded micromachined fiber-optic Fabry-Perot pressure sensors in aerodynamics applications," *IEEE sensors Journal*, vol. 3, no. 1, pp. 102-107, 2003.

[165] J. Xu, X. Wang, K. L. Cooper, G. R. Pickrell, and A. Wang, "Miniature temperature-insensitive Fabry-Pe/spl acute/rot fiber-optic pressure sensor," *IEEE Photonics Technology Letters*, vol. 18, no. 10, pp. 1134-1136, 2006.

[166] Y. Zhang, L. Yuan, X. Lan, A. Kaur, J. Huang, and H. Xiao, "High-temperature fiber-optic Fabry–Perot interferometric pressure sensor fabricated by femtosecond laser," *Optics letters*, vol. 38, no. 22, pp. 4609-4612, 2013.

[167] J. Yin *et al.*, "Batch-producible fiber-optic Fabry–Pérot sensor for simultaneous pressure and temperature sensing," *IEEE Photonics Technology Letters*, vol. 26, no. 20, pp. 2070-2073, 2014.

[168] J. Li *et al.*, "Batch-producible all-silica fiber-optic Fabry–Perot pressure sensor for high-temperature applications up to 800° C," *Sensors and Actuators A: Physical*, vol. 334, p. 113363, 2022.

[169] Y. Zhu and A. Wang, "Miniature fiber-optic pressure sensor," *IEEE Photonics Technology Letters*, vol. 17, no. 2, pp. 447-449, 2005.

[170] Y. Zhu, K. L. Cooper, G. R. Pickrell, and A. Wang, "High-temperature fiber-tip pressure sensor," *Journal of lightwave technology*, vol. 24, no. 2, p. 861, 2006.

[171] E. Cibula, S. Pevec, B. Lenardič, E. Pinet, and D. Đonlagić, "Miniature all-glass robust pressure sensor," *Optics express*, vol. 17, no. 7, pp. 5098-5106, 2009.

[172] J. Xu *et al.*, "Suppression of parasitic interference in a fiber-tip Fabry-Perot interferometer for high-pressure measurements," *Optics Express*, vol. 26, no. 22, pp. 28178-28186, 2018.

[173] X. Wang, J. Xu, Y. Zhu, K. L. Cooper, and A. Wang, "All-fused-silica miniature optical fiber tip pressure sensor," *Optics letters*, vol. 31, no. 7, pp. 885-887, 2006.

[174] Z. Li *et al.*, "Microbubble-based fiber-optic Fabry–Perot pressure sensor for high-temperature application," *Applied Optics*, vol. 57, no. 8, pp. 1738-1743, 2018.

[175] S. Zhang *et al.*, "An Optical Fiber Fabry–Perot Pressure Sensor with Optimized Thin Microbubble Film Shaping for Sensitivity Enhancement," *Coatings*, vol. 10, no. 4, p. 358, 2020.

[176] J. Liu *et al.*, "Fiber-optic Fabry–Perot pressure sensor based on low-temperature co-fired ceramic technology for high-temperature applications," *Applied optics*, vol. 57, no. 15, pp. 4211-4215, 2018.

[177] W. Li *et al.*, "Fiber-optic Fabry–Perot pressure sensor based on sapphire direct bonding for high-temperature applications," *Applied Optics*, vol. 58, no. 7, pp. 1662-1666, 2019.

[178] J. Liu *et al.*, "MgO single crystals MEMS-based fiber-optic Fabry–Perot pressure sensor for harsh monitoring," *IEEE Sensors Journal*, vol. 21, no. 4, pp. 4272-4279, 2020.

[179] P. Jia *et al.*, "Batch-producible MEMS fiber-optic Fabry–Perot pressure sensor for high-temperature application," *Applied Optics*, vol. 57, no. 23, pp. 6687-6692, 2018.

[180] X. Qi *et al.*, "Fiber optic Fabry-Perot pressure sensor with embedded MEMS micro-cavity for ultra-high pressure detection," *Journal of Lightwave Technology*, vol. 37, no. 11, pp. 2719-2725, 2018.

[181] X. Guo, J. Zhou, C. Du, and X. Wang, "Highly sensitive miniature all-silica fiber tip Fabry–Pérot pressure sensor," *IEEE Photonics Technology Letters*, vol. 31, no. 9, pp. 689-692, 2019.

[182] X. Wang, J. Jiang, S. Wang, K. Liu, and T. Liu, "All-silicon dual-cavity fiber-optic pressure sensor with ultralow pressure-temperature cross-sensitivity and wide working temperature range," *Photonics Research*, vol. 9, no. 4, pp. 521-529, 2021.

[183] S. Wang *et al.*, "An Infrasound Sensor Based on Extrinsic Fiber-Optic Fabry–Perot Interferometer Structure," (in en), *IEEE Photonics Technology Letters*, vol. 28, no. 11, pp. 1264-1267, 2016-6-1 2016, doi: 10.1109/LPT.2016.2538318.

[184] L. Liu *et al.*, "Fiber-Optic Michelson Interferometric Acoustic Sensor Based on a PP/PET Diaphragm," (in en), *IEEE Sensors Journal*, vol. 16, no. 9, pp. 3054-3058, 5/2016 2016, doi: 10.1109/JSEN.2016.2526644.

[185] Z. Gong *et al.*, "High-Sensitivity Fabry-Perot Interferometric Acoustic Sensor for Low-Frequency Acoustic Pressure Detections," (in en), *Journal of Lightwave Technology*, vol. 35, no. 24, pp. 5276-5279, 2017-12-15 2017, doi: 10.1109/JLT.2017.2761778.

[186] F. Xu, J. Shi, K. Gong, H. Li, R. Hui, and B. Yu, "Fiber-optic acoustic pressure sensor based on large-area nanolayer silver diaghragm," (in en), *Optics Letters*, vol. 39, no. 10, p. 2838, 2014-05-15 2014, doi: 10.1364/OL.39.002838.

[187] P. Fan *et al.*, "High sensitivity fiber-optic Michelson interferometric low-frequency acoustic sensor based on a gold diaphragm," (in en), *Optics Express*, vol. 28, no. 17, p. 25238, 2020-08-17 2020, doi: 10.1364/OE.402099.

[188] B. Liu *et al.*, "Optical Fiber Fabry–Perot Acoustic Sensors Based on Corrugated Silver Diaphragms," (in en), *IEEE Transactions on Instrumentation and Measurement*, vol. 69, no. 6, pp. 3874-3881, 6/2020 2020, doi: 10.1109/TIM.2019.2939766.

[189] W. Ni *et al.*, "Ultrathin graphene diaphragm-based extrinsic Fabry-Perot interferometer for ultra-wideband fiber optic acoustic sensing," (in en), *Optics Express*, vol. 26, no. 16, p. 20758, 2018-08-06 2018, doi: 10.1364/OE.26.020758.

[190] J. Ma, H. Xuan, H. L. Ho, W. Jin, Y. Yang, and S. Fan, "Fiber-Optic Fabry–Pérot Acoustic Sensor With Multilayer Graphene Diaphragm," (in en), *IEEE Photonics Technology Letters*, vol. 25, no. 10, pp. 932-935, 5/2013 2013, doi: 10.1109/LPT.2013.2256343.

[191] X. Fu *et al.*, "Micromachined extrinsic Fabry-Pérot cavity for low-frequency acoustic wave sensing," (in en), *Optics Express*, vol. 27, no. 17, p. 24300, 2019-08-19 2019, doi: 10.1364/OE.27.024300.

[192] Z. Qu *et al.*, "Low-frequency acoustic Fabry–Pérot fiber sensor based on a micromachined silicon nitride membrane," (in en), *Chinese Optics Letters*, vol. 18, no. 10, p. 101201, 2020 2020, doi: 10.3788/COL202018.101201.

[193] K. Chen, Q. Yu, Z. Gong, M. Guo, and C. Qu, "Ultra-high sensitive fiber-optic Fabry-Perot cantilever enhanced resonant photoacoustic spectroscopy," (in en), *Sensors and Actuators B: Chemical*, vol. 268, pp. 205-209, 09/2018 2018, doi: 10.1016/j.snb.2018.04.123.

[194] M. Guo *et al.*, "Ultrahigh Sensitivity Fiber-Optic Fabry–Perot Interferometric Acoustic Sensor Based on Silicon Cantilever," (in en), *IEEE Transactions on Instrumentation and Measurement*, vol. 70, pp. 1-8, 2021 2021, doi: 10.1109/TIM.2021.3101573.

[195] X. Zhao *et al.*, "Ultra-high sensitive photoacoustic gas detector based on differential multi-pass cell," (in en), *Sensors and Actuators B: Chemical*, vol. 368, p. 132124, 10/2022 2022, doi: 10.1016/j.snb.2022.132124.

[196] K. Chen, Z. Yu, Z. Gong, and Q. Yu, "Lock-in white-light-interferometry-based all-optical photoacoustic spectrometer," (in en), *Optics Letters*, vol. 43, no. 20, p. 5038, 2018-10-15 2018, doi: 10.1364/OL.43.005038.

[197] K. Chen *et al.*, "Highly sensitive optical fiber photoacoustic sensor for in situ detection of dissolved gas in oil," *IEEE Transactions on Instrumentation and Measurement*, vol. 70, pp. 1-8, 2021.

[198] C. Li, M. Guo, B. Zhang, C. Li, B. Yang, and K. Chen, "Miniature single-fiber photoacoustic sensor for methane gas leakage detection," (in en), *Optics and Lasers in Engineering*, vol. 149, p. 106792, 02/2022 2022, doi: 10.1016/j.optlaseng.2021.106792.

[199] Z. Gong, K. Chen, Y. Yang, X. Zhou, W. Peng, and Q. Yu, "High-sensitivity fiber-optic acoustic sensor for photoacoustic spectroscopy based traces gas detection," (in en), *Sensors and Actuators B: Chemical*, vol. 247, pp. 290-295, 08/2017 2017, doi: 10.1016/j.snb.2017.03.009.

[200] Y. Ma, Y. He, Y. Tong, X. Yu, and F. K. Tittel, "Quartz-tuning-fork enhanced photothermal spectroscopy for ultra-high sensitive trace gas detection," (in en), *Optics Express*, vol. 26, no. 24, p. 32103, 2018-11-26 2018, doi: 10.1364/OE.26.032103.

[201] Y. Pan *et al.*, "All-optical light-induced thermoacoustic spectroscopy for remote and non-contact gas sensing," (in en),

Photoacoustics, vol. 27, p. 100389, 09/2022 2022, doi: 10.1016/j.pacs.2022.100389.

[202] P. Zhang *et al*., "An ultra-sensitive magnetic field sensor based on extrinsic fiber-optic Fabry–Perot interferometer and Terfenol-D," *Journal of Lightwave Technology*, vol. 33, no. 15, pp. 3332-3337, 2015.

[203] X.-x. Wang, Y. Zhao, R.-q. Lv, and H.-k. Zheng, "Optic-fiber vector magnetic field sensor utilizing magneto-shape effect of magnetic fluid," *Measurement*, p. 111829, 2022.

[204] Y. Zhao, X.-x. Wang, R.-q. Lv, H.-k. Zheng, Y.-f. Zhou, and M.-q. Chen, "Reflective highly sensitive Fabry–Perot magnetic field sensor based on magneto-volume effect of magnetic fluid," *IEEE Transactions on Instrumentation and Measurement*, vol. 70, pp. 1-6, 2021.

[205] C.-L. Lee, W.-Y. Hong, H.-J. Hsieh, and Z.-Y. Weng, "Air gap fiber Fabry–Pérot interferometer for highly sensitive micro-airflow sensing," *IEEE Photonics Technology Letters*, vol. 23, no. 13, pp. 905-907, 2011.

[206] A. D. Gomes, J. Kobelke, J. Bierlich, K. Schuster, H. Bartelt, and O. Frazao, "Optical fiber probe viscometer based on hollow capillary tube," *Journal of Lightwave Technology*, vol. 37, no. 18, pp. 4456-4461, 2019.

[207] L. H. Chen *et al*., "Chitosan based fiber-optic Fabry–Perot humidity sensor," *Sensors and Actuators B: Chemical*, vol. 169, pp. 167-172, 2012.

[208] C. Li, X. Yu, W. Zhou, Y. Cui, J. Liu, and S. Fan, "Ultrafast miniature fiber-tip Fabry–Perot humidity sensor with thin graphene oxide diaphragm," *Optics letters*, vol. 43, no. 19, pp. 4719-4722, 2018.

[209] C. Bian *et al*., "Optical fiber humidity sensor based on the direct response of the polyimide film," *Applied Optics*, vol. 57, no. 2, pp. 356-361, 2018.

[210] N. Wu *et al.*, "Microwave photonics interrogation for multiplexing fiber Fabry-Perot sensors," *Optics Express*, vol. 29, no. 11, pp. 16652-16664, 2021.

[211] L. R. Chen, M.-I. Comanici, P. Moslemi, J. Hu, and P. Kung, "A review of recent results on simultaneous interrogation of multiple fiber Bragg grating-based sensors using microwave photonics," *Applied Sciences*, vol. 9, no. 2, p. 298, 2019.

[212] Y. Wang, X. Ni, M. Wang, Y. Cui, and Q. Shi, "Demodulation of an optical fiber MEMS pressure sensor based on single bandpass microwave photonic filter," *Optics express*, vol. 25, no. 2, pp. 644-653, 2017.

[213] L. Hua *et al.*, "Distributed Acoustic Sensing Based on Coherent Microwave Photonics Interferometry," *Sensors*, vol. 21, no. 20, p. 6784, 2021.

[214] J. Huang, X. Lan, M. Luo, and H. Xiao, "Spatially continuous distributed fiber optic sensing using optical carrier based microwave interferometry," *Optics express*, vol. 22, no. 15, pp. 18757-18769, 2014.

[215] C. Zhu, M. Roman, Y. Zhuang, and J. Huang, "Distributed fiber optic sensing with enhanced sensitivity based on microwave-photonic Vernier effect," *Optics Letters*, vol. 47, no. 11, pp. 2810-2813, 2022.

[216] J. Huang, L. Hua, X. Lan, T. Wei, and H. Xiao, "Microwave assisted reconstruction of optical interferograms for distributed fiber optic sensing," *Optics express*, vol. 21, no. 15, pp. 18152-18159, 2013.

[217] C. Zhu, R. E. Gerald, and J. Huang, "Progress toward sapphire optical fiber sensors for high-temperature applications," *IEEE Transactions on Instrumentation and measurement*, vol. 69, no. 11, pp. 8639-8655, 2020.

[218] C. Zhu, Y. Chen, Y. Zhuang, and J. Huang, "Displacement and strain measurement up to 1000 C using a hollow coaxial cable Fabry-Perot resonator," *Sensors*, vol. 18, no. 5, p. 1304, 2018.

[219] C. Zhu, R. E. Gerald, Y. Chen, and J. Huang, "Probing the theoretical ultimate limit of coaxial cable sensing: Measuring nanometer-scale displacements," *IEEE Transactions on Microwave Theory and Techniques*, vol. 68, no. 2, pp. 816-823, 2019.

[220] C. Zhu, R. E. Gerald, and J. Huang, "Microwave device inspired by fiber-optic extrinsic Fabry-Perot interferometer: a novel ultra-sensitive sensing platform," *Journal of Lightwave Technology*, vol. 38, no. 24, pp. 6961-6966, 2020.

Chen Zhu (M'18, IEEE) received the B.E. degree in optoelectronics information engineering from the Huazhong University of Science and Technology, Wuhan, China, in 2015, and the Ph.D. degree in electrical engineering from the Missouri University of Science and Technology, MO, USA, in 2021.

He is a Principal Investigator with the Research Center for Optical Fiber Sensing, Zhejiang Lab, Hangzhou 311100, China. He was an Assistant Research Professor with the Department of Electrical and Computer Engineering, Missouri University of Science and Technology. His research interest is focused on the development of fiber optic and microwave devices for sensing applications in harsh environments.

Dr. Zhu was a recipient of the IEEE Instrumentation and Measurement Society Graduate Fellowship Award from 2018 to 2019 and the 2020 IEEE St. Louis Section Outstanding Graduate Student Award. He has authored or co-authored over 50 refereed articles, 10 conference papers, and 1 book chapter.